Partial solvation of lithium ions enhances conductivity in a nanophase-separated polymer electrolyte

Daniel L. Vigil,[†] Benjamin T. Ferko,[‡] Anne Saumer,[¶] Stefan Mecking,[¶] Mark J. Stevens,[*,†] Karen I. Winey,[*,‡,§] and Amalie L. Frischknecht[*,†]

†*Center for Integrated Nanotechnologies, Sandia National Laboratories, Albuquerque, NM, 87185*

‡*Department of Materials Science, University of Pennsylvania*

¶*Department of Chemistry, University of Konstanz, 78457 Konstanz, Germany*

§*Department of Chemical and Biomolecular Engineering, University of Pennsylvania*

E-mail: msteve@sandia.gov; winey@seas.upenn.edu; alfrisc@sandia.gov

Abstract

We demonstrate that a multiblock lithium-ion-conducting polymer can be swollen with ethylene carbonate solvent to increase the conductivity relative to the dry polymer material by nearly four orders of magnitude. This increase is due to partial solvation of lithium ions by ethylene carbonate, which leads to Li^+ diffusion along the solvent-polymer interface. This differs from the vehicular transport mechanism for lithium ions in pure solvent. We use a combination of broadband dielectric spectroscopy, X-ray scattering, and all-atom molecular dynamics simulations to probe the effect of the solvent on the polymer morphology and to elucidate the mechanism of lithium ion transport.

Introduction

Safe, efficient, and reliable batteries are critical to the future of an electricity-based society. A critical component of commercially-relevant batteries is the electrolyte and new electrolyte materials are necessary for next-generation batteries.[1–3] Synthetic polymers have been suggested as one possibility as they have excellent mechanical and chemical stability, and some can dissolve lithium salts. There are a variety of polymer chemistries that have been proposed for electrolyte uses, from simple salt-doped polyethylene oxide (PEO)[4] to polymerized ionic liquids.[5–7] One issue with polymer electrolytes like PEO is they often have a low transference number, which means that much of the ionic conductivity is due to anion motion rather than the desired transport of Li^+.[8,9] One solution to this issue is to use polymers that contain anions either in the backbone or in covalently bonded side chains. When combined with Li^+ ions these polyanions can form materials that allow transport of Li^+without conducting anions due to the slow dynamics of the polymers, leading to transference numbers near unity. Such materials are referred to as single-ion-conducting polymer electrolytes (SIPEs).[5]

Thus far SIPEs have insufficient ionic conductivities to be useful as battery electrolytes.[10] This is presumably due to the strong coupling between Li^+ and the polyanion, which relaxes very slowly, leading to slow Li^+ dynamics.[11] One approach to overcome this issue is to introduce solvent to decouple the Li^+ ions from the polyanion.[12]

In carbonate and glyme bulk liquid electrolytes, the organic solvent usually fully coordinates Li^+ and the Li^+ ions diffuse with their solvent shell.[13–15] This so-called vehicular transport may allow for much faster diffusion of Li^+ in solvent-swollen polymer electrolytes due to the higher mobility of the small molecule solvent compared to the polymer.[16]

Added solvent may also enhance polymer segment mobility by disrupting polymer-polymer associations. These associations can occur when two anionic or polar groups on different polymer chains are associated to the same Li^+ ion, creating a physical crosslink. Added solvent may disrupt these transient crosslinks by displacing some of the polymer-Li^+ interactions, which will lead to faster polymer segmental dynamics, and possibly faster Li^+ diffusion.

Specifically, the solvent enhances Li+ mobility by reducing the energetic barrier for Li^+ to dissociate from the polymer. Quantum chemistry calculations have shown that Li^+ forms strong associations with sulfonate (SO_3^-) groups, which is a common moiety in anion-containing polymers.[11] The strong binding energy between SO_3^- and Li^+ leads to a large activation barrier for Li^+ to escape associations with SO_3^- groups.[11] Added solvent may displace some of these strong Li^+-SO_3^- interactions and create short-lived transition states where Li^+ is mostly associated to solvent and can change SO_3^- associations with only modest energy barriers. We refer to this mechanism as barrier reduction by partial solvation.

While introducing solvent may help increase Li^+ mobility in SIPEs through the various mechanisms just discussed, added solvent can also disrupt the mechanical properties of these materials. To mitigate this issue, block copolymers and selective solvents can be combined to achieve both high ion conductivity and mechanical strength.[17] Block copolymers self-assemble into spatially separated domains, which in the case of block ionomers are typically polar and non-polar. Ideally the solvent will selectively swell the polar domains and increase ionic conductivity. The non-polar domains will ideally remain free of solvent and provide the desired mechanical properties for battery applications.

Some of our previous work has demonstrated the potential of single-ion-conducting block copolymers. In particular, we have investigated a set of strictly-alternating multiblock copolymers based on short aliphatic and sulfosuccinate groups that self assemble into an array of morphologies, including layers, hexagonally packed cylinders, and double gyroid.[18–21] These surfactant-like multiblock polymers have short blocks and strong interactions, leading to relatively small domain spacings on the order of a few nanometers. In the dry state these polymers have low but measurable ion conductivities that depend on the nano-phase separated morphology. It was further shown that DMSO could selectively swell the polar domains and increase ion conductivity. [22] Unfortunately, DMSO has limited utility in battery cells as it binds Li^+ ions strongly and can intercalate into the cathode with Li^+ ions.[23]

In this work we demonstrate that the industry-standard ethylene carbonate solvent can

be added in small amounts to single-ion-conducting multiblock copolymers to increase the conductivity of Li^+ by almost four orders of magnitude. We use a combination of experiments and computational simulations to elucidate the impact of the added solvent on the polymer morphology and the local environment of the Li^+ ions. Rather than observing vehicular diffusion with a full solvent shell that occurs in pure solvent electrolytes, we provide evidence for a Li^+ transport mechanism that is localised to the polymer-solvent interface.

Experimental Methods

Materials

All experiments and simulations in this work use an ion-containing multiblock copolymer, PES12Li, consisting of an exactly 12-carbon linear alkane nonpolar block strictly alternating with a lithium sulfosuccinate ester polar block (Figure 1). Synthetic procedure, molecular weight, and morphologies have been previously reported.[20] Ethylene carbonate (EC) was purchased from Sigma-Aldrich and used directly as the swelling solvent. The water concentration of the solvent was determined to be approximately 150 ppm by Karl Fischer titration.

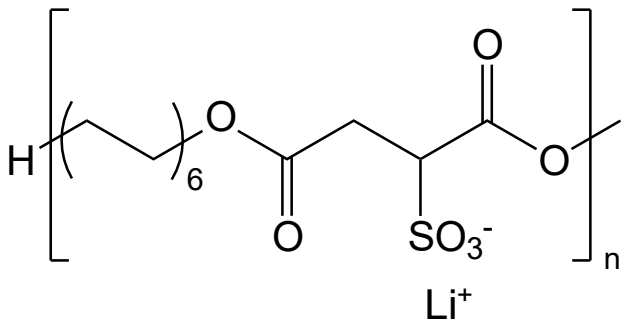

Figure 1: Chemical structure of PES12Li multiblock copolymer. The sulfonate group (SO^-_3) can be located on either of the α-ester carbons.

Sample Preparation

Dried membranes were prepared prior to swelling by hot-pressing dry PES12Li (T_m = 75°C) at 90°C with 2 tons of pressure in air for 15 minutes, resulting in thicknesses of 100-200 microns. Residual moisture was removed by drying under vacuum at 90 °C for 12 hours.

Some of the membranes were briefly heated to 135°C ($T > T_{ODT}$) and annealed under vacuum at 60°C until a layered morphology was observed by X-ray scattering. We refer to this step as post-press annealing. This step was necessary to achieve a well equilibrated nanophase morphology for some samples. We suspect that the high χ parameter and multi-block architecture make large scale chain rearrangements prohibitively slow in the ordered state. Traversal of the order-disorder transition facilitates access to a more equilibrated layer structure with a domain spacing slightly smaller than previously reported.[20]

All membranes were transferred into a nitrogen glovebox and were further dried (vacuum, 85°C, 30 minutes) to remove any moisture accumulated during the transfer.

For samples with incorporated solvent, swelling was performed in the glovebox by briefly heating the dry membrane to 90°C to melt the crystalline nonpolar domains, then immersing molten membranes in EC at 90°C for 5 minutes to 6 hours. Swelling time was used to control the amount of solvent incorporated into the membrane. Following swelling, residual solvent was removed by dabbing the samples with tissues before the membranes were diced for use in experiments. All membranes were 100-200 microns thick after swelling.

Solvent Uptake Measurements

Thermogravimetric analysis (TGA) was performed using a Netzsch STA 449 F5 Jupiter or TA Instruments Discovery SDT 650. Both dry and solvent-swollen membranes were heated under flowing air (100 sccm) from room temperature to 400°C or 500°C with a heating rate of 10°C/min. The solvent weight fractions (w_s) of the swollen membranes were calculated by comparing the mass loss of a swollen membrane to a dry membrane before the onset of polymer degradation (Figure S1). Solvent uptake is quantified by the solvation number,

which is the number of solvent molecules per Li^+ present in the sample. The solvation number is calculated from the TGA data by:

$$\lambda = \frac{M_0 \quad w_S}{M_S\,(1 - w_S)} \tag{1}$$

where M_0 is the repeat unit (Figure 1) molecular weight and M_S is the molecular weight of the EC solvent. Five unique λ values were achieved. Table S1 shows the sample preparation and swelling times that were used to achieve each λ value.

X-ray Scattering

X-ray scattering was performed at the Dual Source and Environmental X-ray Scattering (DEXS) facility at the University of Pennsylvania. The DEXS facility houses a Xeuss 2.0 equipped with a PILATUS 1 M detector for small- angle scattering (SAXS), a PILATUS 100K detector for wide-angle scattering (WAXS), and a GeniX3D beam source (8 keV, CuKα, λ = 1.54 Å). Dry membranes were used directly, and swollen membranes were sealed in 1.0 mm diameter glass capillaries (Charles Supper Company) under nitrogen within the glove box. For measurements above room temperature, samples were equilibrated at the target temperature for 10 minutes prior to 10 minute exposures. The sample-to-detector distances were approximately 360 mm for SAXS and 150 mm for WAXS. 2D patterns were isotropic and azimuthally integrated to yield 1D I(q) plots.

Dielectric Relaxation Spectroscopy (DRS)

Dried membranes were prepared by sandwiching the material between two polished stainless steel electrodes and holding the sample above the melting temperature under vacuum to ensure good wetting of the electrodes. Glass fiber spacers were used to fix the spacing between the electrodes at 100 μm. Swollen membranes were sandwiched between stainless steel electrodes and crimped into hermetically sealed coin cells within the glovebox. Isothermal

frequency sweeps between 0.1-10^6 Hz were performed using a Solartron Modulab XM with a 100 mV AC amplitude. Equilibration at the highest measured temperature was ensured by waiting until subsequent frequency sweeps yielded identical results. Data was collected on cooling with temperature steps of 2 K and an equilibration time of 5 minutes at each temperature. Ionic conductivity was determined from the plateau in the in-phase conductivity (σ') spectra. Conductivities were found to be reversible with temperature (Figure S3). Further details of the analysis methods can be found in the Supplementary Information.

Computational Methods

All-atom, fixed-charge molecular dynamics (MD) simulations were conducted using LAMMPS.[24] OPLS-style force fields were used for all molecules. The force field parameters for ethylene carbonate were taken from a recent publication.[25] We use the hydrocarbon model from the L-OPLS force field[26] for the alkane segment and model the sulfonate group with parameters from the CL&P force field. [27] We recently investigated several force field parameters for Li^+ in an organic solvent.[28] We found that the original OPLS parameters for Li^+ lead to overly large coordination numbers as compared with experiment and ab initio calculations. Consistent with this finding, we use Li^+ force field parameters from Wu and Wick. [29] The charges on Li^+ and sulfonate-group atoms were reduced by a factor of 0.78 in accordance with the electronic continuum model of Leontyev,[30–32] which has been shown to lead to more accurate ion dynamics for fixed charge force fields.

All simulations contained 60 polymers with 16 monomeric units per chain, with 960 Li^+ counterions total in the system. The polymers had randomly selected stereochemistry for the sulfosuccinate group. Initial states for the disordered aggregate morphology were constructed using the Monte Carlo code EMC.[33,34] Morphologies consisting of alternating layers of the nonpolar and polar blocks were constructed using a custom python script to place the chains in the simulation box. The nonpolar (alkane) blocks were initially constructed in a crystalline

state. Morphologies with amorphous alkane block layers were obtained by compressing the crystalline layers in the direction perpendicular to the layers while allowing the cell to relax in the dimensions parallel to the layers. For all morphologies, the initial state was equilibrated for 60-400 ns in an NPT ensemble until pressures and simulation cell dimensions stabilized. We used a triclinic cell so that the pressure in each direction was relaxed independently and the cell shape could distort from orthorhombic. A subsequent NVT-ensemble simulation was conducted with at least 10 ns of equilibration followed by at least 100 ns of data collection. All simulations were integrated in time with a velocity Verlet algorithm with a 1 fs timestep and were thermostatted with a Nosé-Hoover thermostat. Simulations in the NPT ensemble used a Nosé-Hoover barostat. Electrostatic interactions were computed with a PPPM method with 10^{-4} accuracy. MD snapshots were rendered with Ovito.[35]

Results and Discussion

Nanoscale Morphology

We first characterize the morphology of the self-assembled materials via X-ray scattering and molecular dynamics (MD) simulations. Figure 2 shows the X-ray scattering intensity for the polymer material in both the dry state and states swollen with EC solvent.

Figure 2(a) shows the scattering intensity for a dry sample that has been annealed above the order-disorder transition ($T_{\mathrm{ODT}} \approx 112^{\circ}C$).[20] The figure shows a single broad peak at low q associated with disordered aggregates and another broad feature at $q > 1\,\mathrm{\AA}^{-1}$. The red curve in Figure 2(a) is a scattering intensity calculated from MD simulations of dry PES12Li with disordered aggregates at 160°C. The scattering intensity was calculated using the procedure described in previous work. [36] Figure 2(f) shows a corresponding snapshot from the MD simulation. There is good agreement between experiment and simulation for the position of the low q peak in Figure 2(a), which indicates that the selected force fields accurately reproduce the structure of the disordered aggregates.

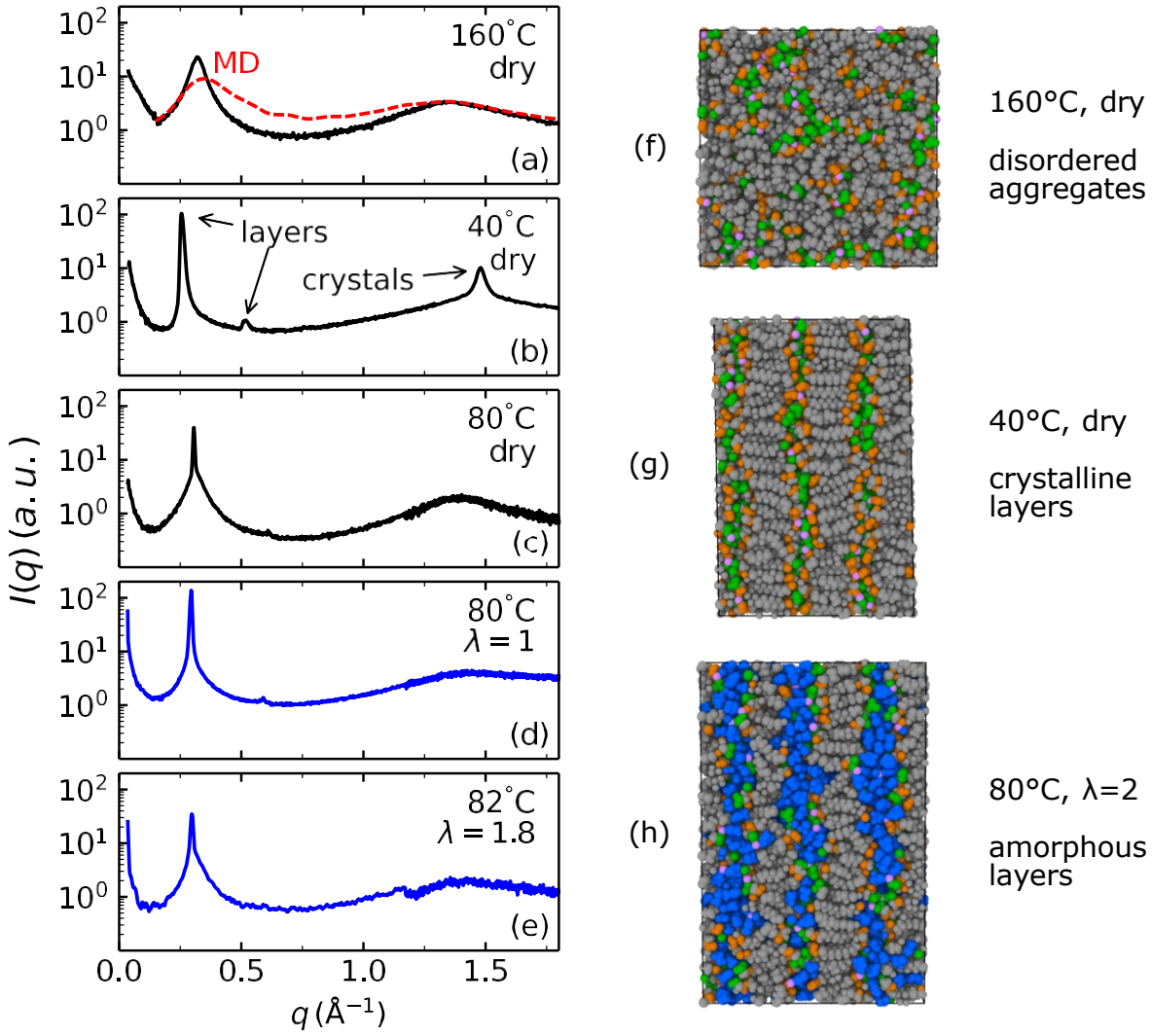

Figure 2: X-ray scattering intensities of dry PES12Li (a,b,c) and EC-swollen PES12Li (d,e) at various temperatures and amounts of added solvent. Scattering intensity from molecular dynamics simulation is shown with a red dashed line in (a). MD simulation snapshots of dry PES12Li with disordered aggregate morphology (f) or crystalline layers (g) and EC-swollen PES12Li with $\lambda = 2$ and amorphous layer morphology (h). EC molecules are shown in blue, hydrocarbon segments are shown in gray, sulfonate groups (SO_3^-) are shown in green, polymer ester group are shown in orange, and Li^+ is shown in purple.

The scattering intensity for a dry PES12Li sample annealed at 40 ◦C is shown in Figure 2(b). The data shows a peak around 1.5 $Å^{-1}$, which is consistent with crystallized polyethylene domains of hexagonal symmetry.[37,38] For $q < 0.7$ $Å^{-1}$, peaks with the ratio $q^* : 2q^*$ indicate a layered morphology with a domain spacing of 23.1 Å. We refer to this morphology as 'crystalline layers.' A snapshot from a MD simulation of dry PES12Li with crystalline

layers at the same temperature as the experiment is shown in Figure 2(g). We reemphasize that all MD simulations of layers were initialized from a layered morphology as the timescale for self-assembly is much longer than is possible with all-atom MD. In the simulations, most of the carbon backbone dihedral angles in the hydrocarbon segment are in the trans configuration and the polar blocks of the polymer form well-defined layers that contain the Li^+ ions.

The same sample was annealed above its melting temperature (T_m = 75°C) and the scattering intensity was remeasured at 80°C, as shown in Figure 2(c). The peak near q = 1.5 $Å^{-1}$ associated with crystalline order in the alkyl domains has disappeared, consistent with an amorphous nonpolar block. Additionally, the peaks at low q maintain the ratio q^* : $2q^*$ for a layered assembly, but have shifted to higher q, indicating a smaller domain spacing of 20.5 Å. This morphology we refer to as 'amorphous layers.' MD simulations of the amorphous layers also indicate a reduced domain spacing compared to the simulations of crystalline layers at 40°C. Additionally, the fraction of trans configuration dihedral angles in the hydrocarbon segment is 7% lower in the amorphous layers compared to the crystalline layers.

Figure 2(d) and (e) display the scattering intensity for samples that were swollen with EC to λ = 1 and λ = 1.8, respectively. The scattering intensities are consistent with amorphous layer morphologies, but have slightly larger domain spacings than that of the dry material shown in Figure 2(c). For the sample with λ = 1.8, a broad feature appears underneath the primary peak and the secondary reflection at $2q^*$ is not apparent, indicating more disordered layers. However, cooling the sample below 80°C removes the broad feature and reveals the secondary reflection, indicating that the sample is undergoing an order-disorder transition (ODT) at this temperature and λ. For the sample with λ = 1, the ODT occurs near 90°C. Figures S4 and S5 show the temperature-dependent X-ray scattering data.

Swelling of the layers by the solvent at 90°C occurs in both the lateral and axial directions. Lateral swelling reduces the driving force for crystallization, and recrystallization of the nonpolar block is not observed in solvent-swollen PES12Li, even when cooled to room

temperature. Other samples with lower values of λ were obtained by swelling the polymer membranes for shorter amounts of time. All samples with $\lambda > 0.25$ formed amorphous layers, while samples with $\lambda \leq 0.25$ formed crystalline layers upon cooling below T_m.

A snapshot from MD simulations of a PES12Li sample with $\lambda = 2$ is shown in Figure 2(h). When compared to part (g) which shows crystalline layers, the hydrocarbon segments (gray) are not as ordered, which is indicative of the amorphous layers. Furthermore, the lateral and axial swelling due to the added solvent are both apparent. Additional snapshots from the MD simulations and analysis of the spatial distribution of SO_3^- groups is shown in Figure S7.

Previous computational work on precise acid-containing polyethylene considered crystalline layers formed either by extended-chain conformations or adjacent-reentry conformations.[38] We simulated both chain conformations for dry PES12Li at 40°C and found that the adjacent-reentry chain conformations produced a layer period (22.0 Å) that was closer to the experimental value (23.1 Å) than extended-chain conformations (17.5 Å). Example snapshots for the extended-chain and adjacent-reentry conformations are shown in Figures S8 and S9, respectively. The adjacent-reentry conformation yields domain spacings that are close to experiments and we speculate that the small difference of $\sim$ 1 Å between simulation and experiment is due to loop and bridge defects which may increase the domain spacing in experiments. These defects are not present in the simulations. We use the defect-free adjacent-reentry conformations for all further MD simulations.

We now quantitatively compare the layered morphologies from the MD simulations to the experimental layered morphologies with added solvent. We note that we do not calculate the scattering intensities from the MD simulations of the layered morphologies because the simulations are inherently anisotropic (due to their small box size), while the experimental X-ray measurements average over a much larger sample and result in isotropic scattering profiles. A more useful comparison is of the spacing between the layers. Figure 3 shows the domain spacing of PES12Li layers with varying amounts of added solvent measured by

SAXS (open symbols) and calculated from MD simulations (filled symbols). The crystalline layers have a larger domain spacing than the amorphous layers due to the orientation of the chains and higher fraction of trans conformation backbone dihedral angles. With MD simulations we are able to create crystalline layers with added solvent up to $\lambda = 2$. For $\lambda = 3$, crystalline layers were not stable in MD simulations.

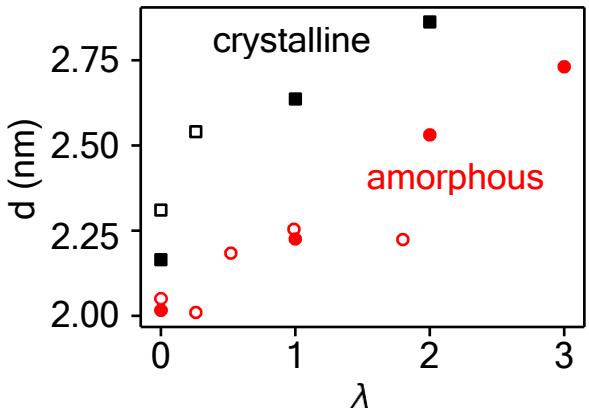

Figure 3: Domain spacing, d, as a function of amount of solvent λ for crystalline layers (black) and amorphous layers (red). Open symbols represent data from small-angle x-ray scattering taken at 40°C and filled symbols represent data from MD simulations at 80°C. Experimental domain spacings decrease by about 0.1 nm between 40°C and 80°C.

There is good agreement in domain spacing between SAXS and MD simulation for the amorphous layers for $\lambda \leq 1$. As solvent is added from $\lambda = 0$ to $\lambda = 1$, both lateral and axial swelling occurs which increases both the domain spacing and area per sulfonate group in the layers. Above $\lambda = 1$, the domain spacing determined from SAXS saturates around 22 Å, whereas in the MD simulations the domain spacing continues to increase. One possibility is that experimentally there are chain segments that bridge between layers, hindering further axial swelling upon adding solvent above $\lambda = 1$. The MD simulations do not contain bridging chains so the domain spacing can increase upon further addition of solvent.

In addition to the domain spacing, we can extract spatial distribution information from the MD simulations. Figure 4 shows the spatial distribution profile of Li^+, EC, and various groups on the polymer as measured perpendicular to the layers. These profiles have been

averaged in the plane of the layers. Figure 4(a) shows the profiles in dry, crystalline layers. This system forms a flat, well defined interface between the polar block of the polymer and the non-polar block. The concentration of polar groups (polymer ester OCO, SO_3^-, Li^+) is zero inside the non-polar domain. Similarly, the concentration of hydrocarbon segments goes to zero in the center of the polar domain formed by Li^+ and SO_3^-. Part (d) shows a single polymer layer from an MD simulation of the dry, crystalline layers with adjacent-reentry packing. The separation between non-polar (gray) and polar (green, orange, purple) groups is evident.

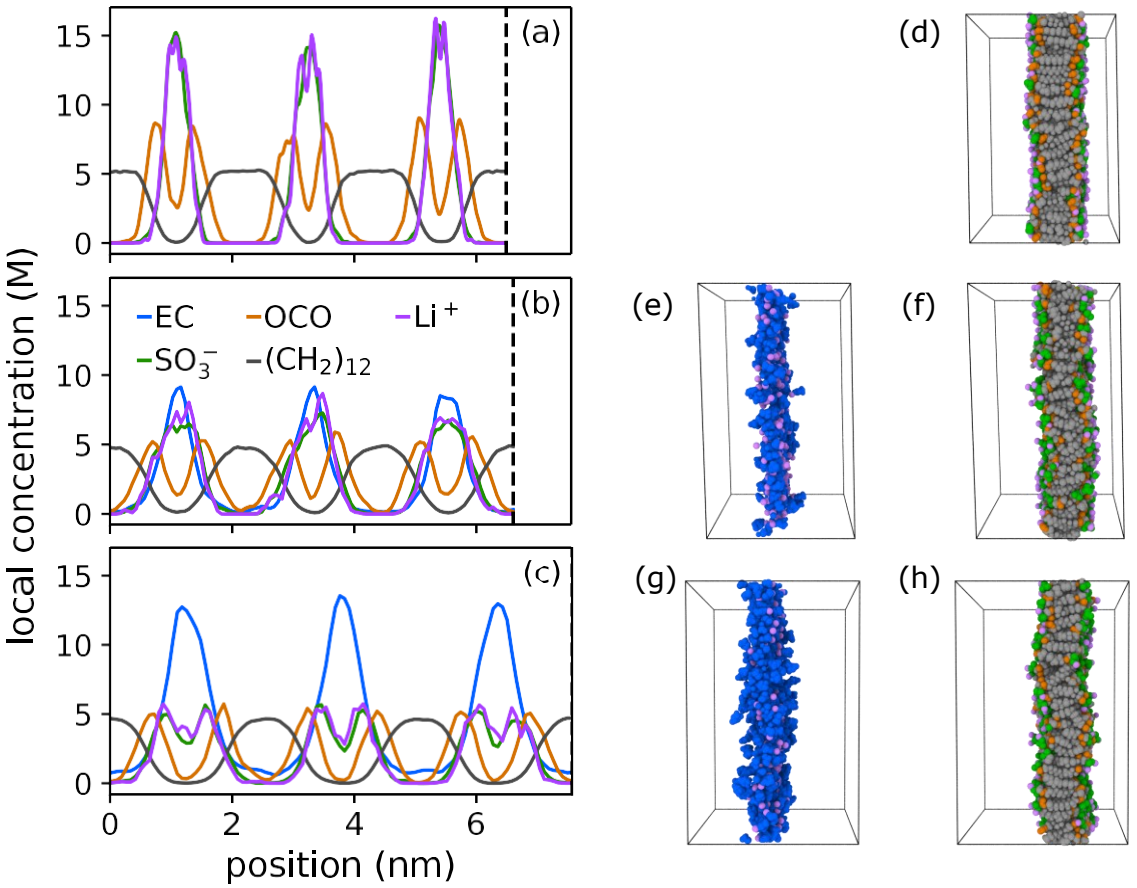

Figure 4: Distribution of various groups along the direction perpendicular to the layers in the layered morphologies at 80°C. The data are for (a) dry, λ = 0, crystalline layers, (b) EC-swollen λ = 1 amorphous layers and (c) λ = 2 amorphous layers. The curve for Li^+ lies almost completely on top of the curve for SO_3^- in parts (a)-(c). Vertical dashed black lines indicate three layer periods. (d),(f), and (h) show a single polymer layer with hydrocarbon segments shown in gray, SO_3^- groups in green, ester groups in orange, and Li^+ in purple. (e) and (g) show a single solvent layer with associated Li^+. Solvent molecules are blue.

Figure 4(a) also shows that the Li^+ and SO^-_3profiles are nearly completely overlapped, indicating strong coordination between Li^+ and SO_3^-. This will be explored further in the next section. The polymer esters (OCO, orange) sit at the interface between the polar domain and the non-polar domain. While the SO^-_3 groups from adjacent polymer layers mix together to form a single polar domain, there are two clear peaks in the OCO profile from the two opposing polymer layers. There is some overlap between the OCO and Li^+ concentration, and we will see later that Li^+-OCO associations are common. This can also be seen in part (d) where the green SO^-_3 groups are more accessible to the purple Li^+ ions, whereas some of the orange OCO groups are buried more towards the non-polar domain, though Li^+ does still associate with the orange OCO groups.

Figure 4(b) shows the distribution of the same groups, but in an EC-swollen system with $\lambda = 1$ and amorphous layers. The added EC is located completely within the polar domain. There is still strong separation between the polar groups (OCO, SO_3^-, EC, Li^+) and the non-polar hydrocarbon segments, however the interface between the polar and non-polar domains is broader in Figure 4(b) compared to part (a). Figure 4(e) and (f) show single layers of solvent and polymer, respectively, with the Li^+ ions that are associated with each. Many of the Li^+ ions are located at the interface between the solvent and the polymer layer and appear in both images. The solvent layer is not perfectly flat, which in turn causes the polymer layer to be slightly irregular compared to the dry system in part (d). This accounts for the broadened interface between polar and non-polar groups seen in part (b) when compared to part (a).

Figure 4(c) shows the spatial distribution of EC, Li^+, and polymer groups for $\lambda = 2$ in amorphous layers. At this level of added solvent the EC no longer resides solely within the polar domain. A small fraction of EC moves into the non-polar domain, as seen in Figure 4(c) by the non-zero value of the EC concentration in the non-polar region. This is also consistent with SAXS measurements, as the primary peak for the sample with $\lambda = 1.8$ has an underlying broad feature that is not present in the $\lambda = 1$ sample, which indicates that

the $\lambda = 1.8$ sample is less well ordered. So much EC has been added that the Li^+ and SO_3^- groups no longer form a single peak in each layer, but rather show two peaks. This indicates that adjacent polymer layers are beginning to decouple due to the amount of added solvent between them. Figure 4(g) and (h) show snapshots from MD simulations of the amorphous layers with $\lambda = 2$. The increased width of the solvent layer is apparent.

Ion coordination

In the previous section we showed that PES12Li forms well ordered layers with non-polar domains of alkane segments and polar domains of Li^+, SO_3^-, OCO groups and EC, if present. The Li^+ tend to sit at the interface between polymer layers in the dry material or at the polymer-EC interface when solvent is added. We now characterize the number and type of associations that Li^+ forms.

We first consider the radial distribution function (RDF) between Li^+ and other elements. Figure S10 in the Supporting Information shows that in the disordered aggregate morphology at $\lambda = 1$, Li^+ has a primary solvation shell composed of oxygen atoms. The number of oxygens in this first shell is four, which can be determined from both the integrated RDF (not shown) and the neighborship ordered RDF (Figure S11), consistent with previous results.[28] All other morphologies and λ values also show 4 oxygens in the primary solvation shell for Li^+.

The types of oxygens that form the first solvation shell varies with λ and morphology. There are five types of oxygens in the system: SO_3^-, etherial ester, carbonyl ester, etherial EC, and carbonyl EC. Figure S12 shows an example of the composition of each neighborship ordered RDF. The etherial ester and etherial EC oxygens are commonly found in the second solvation shell, but are almost never found in the first solvation shell of Li^+, so we focus on the other three oxygen types from here on.

One can compute the average number of SO_3^-, carbonyl ester, and carbonyl EC oxygens in the primary solvation shell of Li^+. We find it more useful, however, to describe the full

distribution of coordination states as there can be large variations in the coordination environments of individual Li^+, from fully coordinated by SO_3^- oxygens to fully coordinated by EC oxygens. Table 1 gives the number fraction of Li^+ with a given number of coordinations to EC, SO_3^- or to the polymer ester (OCO) in an amorphous layered morphology with $\lambda = 3$. The same data for other amounts of added solvent ($\lambda = 1$ or 2) are given in Table S3. These tables only include coordination states that contain at least 1% of the Li^+ ions in the system.

Table 1: Number fraction of Li^+ with a given number of EC, SO_3^-, and ester (OCO) coordinations in amorphous layers with $\lambda = 3$ at 80°C. The mean lifetime ($\bar{\tau}_a$) of each coordination state and the fractional contribution of each state to the total Li^+ displacement ($f_{\Delta r}$) are also given.

n_{EC}	$n_{SO_3^-}$	n_{OCO}	Number fraction	$\bar{\tau}_a$ (ns)	$f_{\Delta r}$
0	3	1	0.019	0.63	0.003
0	2	2	0.015	0.50	0.017
1	3	0	0.094	1.36	0.021
1	2	1	0.117	0.84	0.035
1	1	2	0.042	0.61	0.020
2	2	0	0.214	1.18	0.070
2	1	1	0.137	0.85	0.196
2	0	2	0.023	0.62	0.066
3	1	0	0.200	1.07	0.279
3	0	1	0.051	0.72	0.099
4	0	0	0.054	0.81	0.135

From Table 1 we compute that for $\lambda = 3$, on average a Li^+ is coordinated by 2 EC oxygens, 1.5 SO_3^- oxygens, and 0.5 ester oxygens, however only 37% of Li^+ actually have 2 EC oxygens in the primary solvation shell. Approximately 5% of Li^+ are completely solvated by EC ($n_{EC} = 4$) and 25% of Li^+ have three EC associations and only one polymer association. Almost 29% of Li^+ have three or more polymer associations. The distribution of coordination states is thus broad. Other states were observed that were not included in the table, but they typically accounted for less than 0.2% of the Li^+.

In addition to calculating the number fraction of each state, we calculated the average lifetime of each state, $\bar{\tau}_a$. The data in Table 1 is averaged over 100 ns of simulation time, dur-

ing which individual Li^+ can change their coordination state many times, since the lifetime of each state is of order 1 ns.

Some of the previously mentioned uncommon states that are not listed in the table had short lifetimes ($\bar{\tau}_a < 0.05$ ns) and had 5 oxygens in the primary solvation shell rather than 4. We believe these to be transition states where one oxygen is coming to replace another in the primary solvation. The combined number fraction of all transitions states is less than 3%.

The trends outlined above also occur at lower solvation numbers. Table S3 lists the number fraction of each state for λ = 1 and λ = 2. The average number of polymer associations increases with decreasing amount of solvent, but there is still a broad distribution of states present for all solvation levels. We expect the different coordination states to have different mobilities, which in turn will affect the overall dynamics of Li^+ which we evaluate in the next section. The final column of Table 1 is related to the transport of Li^+ and is explained in the next section.

Dynamics

We measure the conductivity of Li^+ with dielectric relaxation spectroscopy (DRS). Data for dry PES12Li (λ = 0) and the EC-swollen (λ = 1 or 1.8) PES12Li are given in Figure 5(a). For the dry material, the conductivity is only measurable above 100°C. This is close to the order-disorder transition and all of the data is from the disordered aggregate morphology due to slow ordering kinetics.[20] In contrast, the EC-swollen material has measurable conductivity at temperatures where amorphous layers are stable. The addition of EC increases the conductivity at moderate temperatures (70-90°C) by nearly four orders of magnitude compared to the dry material.

We now use dielectric relaxation spectroscopy (DRS) and results from MD simulations to directly evaluate the mechanism(s) of Li^+ transport. Starting with the MD simulations, Figure 6 shows the mean squared displacement (MSD) of various groups in the layered

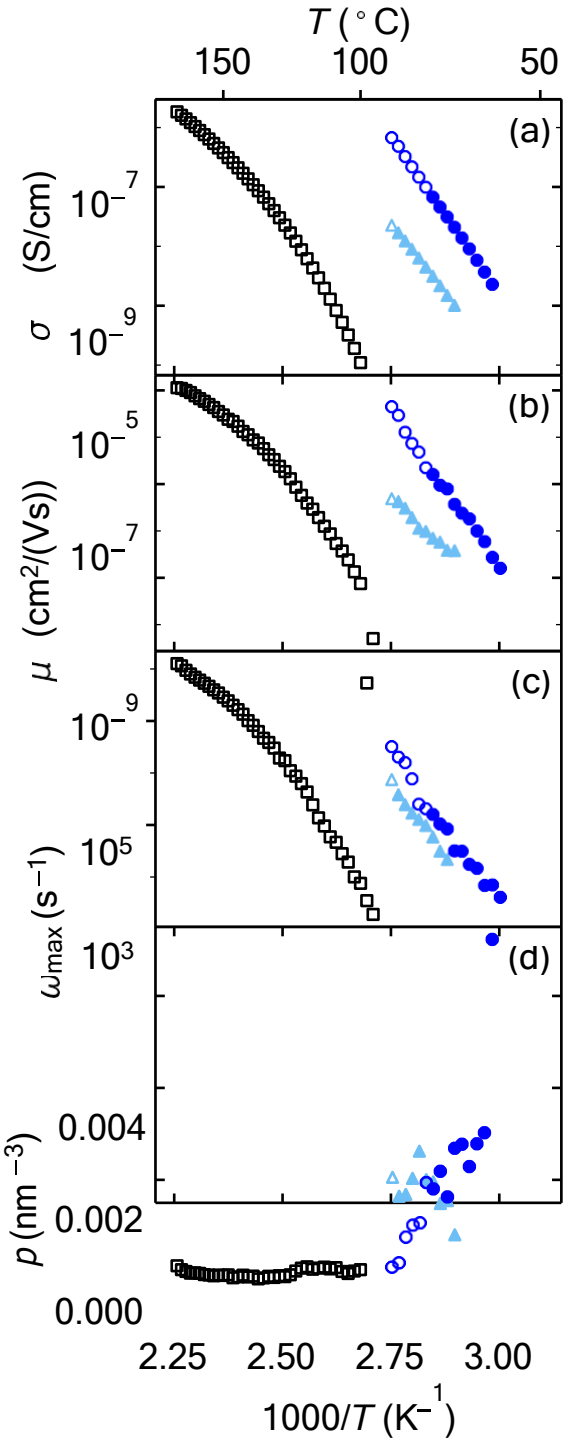

Figure 5: (a) Conductivity of dry PES12Li (black squares) and EC-swollen PES12Li with $\lambda = 1$ (light blue triangles) or $\lambda = 1.8$ (dark blue circles) at various temperatures as measured by DRS. The morphology at each temperature is indicated with open symbols (disordered) or filled symbols (amorphous layers). (b) Mobility of conducting ions. (c) Peak relaxation frequency. (d) Concentration of conducting ions from DRS.

morphologies at 80°C. Part (a) shows data for dry ($\lambda = 0$), crystalline layers, for which there is little motion of either Li^+ (purple), SO^-_3groups (green), or hydrocarbon segments (gray).

In the timescales accessible to all-atom MD (0(10^2 ns)), the groups only move at most 1-2 Å, indicating that all groups are trapped in the cage formed by their local neighbors and do not diffuse on this time scale. Overall, this is consistent with the unmeasurably small conductivity for the dry material at 80°C found in Figure 5(a). Additionally, the MSD for Li^+ and SO_3^- are close together, especially at short times, indicating strong correlations between these two groups.

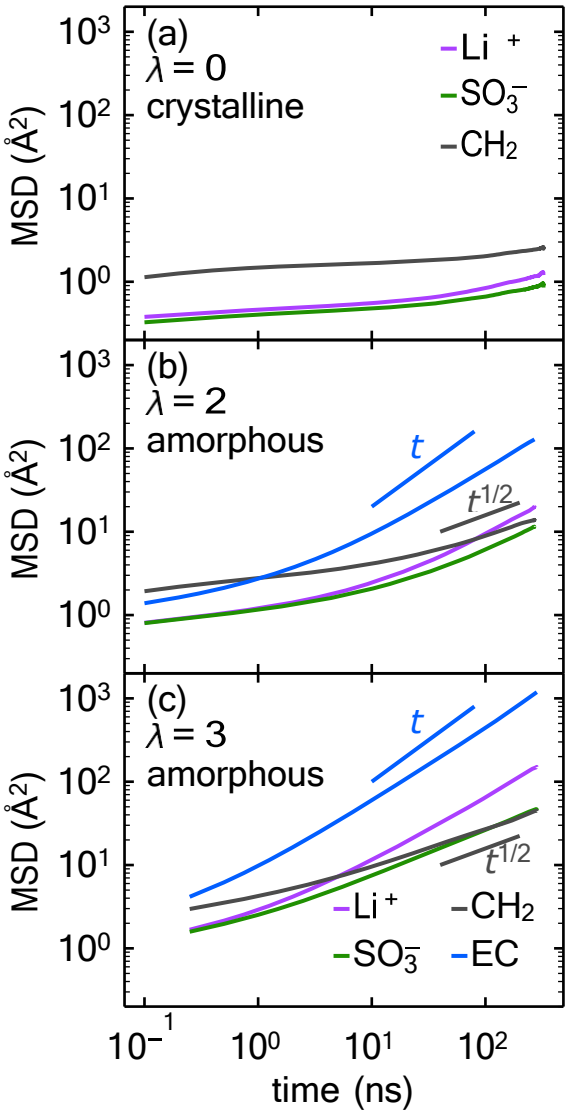

Figure 6: Mean squared displacement (MSD) of various groups in layered morphologies at 80°C from molecular dynamics. (a) Dry PES12Li with crystalline layer morphology. EC-swollen PES12Li with amorphous layer morphology and $\lambda = 2$ (b) or $\lambda = 3$ (c). Line segments labeled with t or $t^{1/2}$ indicate scaling regimes.

In sharp contrast, significant diffusion occurs for various groups in the EC-swollen (λ = 2 or 3), amorphous layer morphology as shown in Figure 6(b) and (c). The Li^+ ions are able to move tens of Å for λ = 3 and their MSD approaches diffusive scaling at long times. The Li^+ also move significantly faster than the SO_3^- groups, which implies that Li^+ motion is separated from the SO_3^- groups and the polymer, in general, at sufficiently long time scales. The MSDs for polymer groups (nonpolar groups and the sulfonate groups) converge at long times and show a subdiffusive scaling $t^{1/2}$ consistent with Rouse dynamics.

The enhanced mobility of Li^+ with added solvent is also seen from DRS. Figure 5(b) shows the mobility of conducting ions (Li^+), which increases by orders of magnitude as λ is increased from 0 to 1 to 1.8. This is in qualitative agreement with MD simulations.

Figure 6 also shows that the MSD of the polymer increases with increasing amount of solvent. This indicates that added solvent enhances polymer segment mobility for this system. We note that for the SO_3^- groups, the mobility represents a wiggling motion in the plane of the layers, which is observed from the MD trajectories.

We also find evidence for increased polymer segment mobility from DRS. From DRS, we are able to extract a relaxation frequency ω_{max} that is related to the relaxation of the polymer (details provided in the SI). [39,40] This data is plotted in Figure 5(c). The relaxation frequency ω_{max} is significantly higher for the solvent swollen samples compared to the dry material, consistent with enhanced segmental mobility. However, there is a minor increase in segmental mobility as λ is increased from 1 to 1.8. This suggests that the measured conductivity increase is due to more than this factor alone.

Returning to the MSD displacement data in Figure 6, we see that the EC molecules move significantly faster than either the Li^+ or polymer. As shown previously in the ion coordination analysis, the EC is partially solvating a significant fraction of the Li^+, and the EC is mobile in the system. Thus, EC is providing a new pathway for Li^+ diffusion with respect to the dry polymer system.

To evaluate the connection between ion coordination and diffusion, we compute the total

displacement of Li^+ over the entire simulation, Δr_{tot}, then decompose it into contributions from each coordination state, $\Delta r(n_{EC}, n_{SO_3^-}, n_{OCO})$. We then define the displacement fraction as

$$f_{\Delta r}(X) = \Delta r(X)/\Delta r_{tot}, \quad (2)$$

where $X = \{n_{EC}, n_{SO_3^-}, n_{OCO}\}$ represents a given coordination state. This equation characterizes the fraction of the total Li^+ displacement that occurs in a given coordination state. For $\lambda = 3$, $f_{\Delta r}$ is given for each coordination state in Table 1. For lower values of λ, the Li^+ did not diffuse sufficiently far to obtain consistent values of $f_{\Delta r}$.

Table 1 shows that the fully solvated coordination state ($n_{EC} = 4$, $n_{SO_3^-} = n_{OCO} = 0$), despite only accounting for 5.4% of Li^+ when $\lambda = 3$, accounts for 13.5% of the total displacement. This indicates that the fully solvated state is indeed more mobile than other states, but it does not account for a majority of the total Li^+ transport.

The majority of the displacement of Li^+ occurs in states with $n_{EC} = 2$ or 3 and $n_{SO_3^-} \leq 1$. These Li^+ states are all partially solvated but are still coordinated to the polymer. Each of these states accounts for a larger fraction of the total displacement than they contribute to the number fraction of states ($f_{\Delta r}$ > number fraction), which indicates these have above average mobility. We refer to these states with $n_{EC} = 2$ or 3 and $n_{SO_3^-} \leq 1$ as mobile, partially-solvated states.

The least mobile states are those with three or more polymer associations or two or more SO_3^- associations. The coordination states with three or more polymer associations ($n_{SO_3^-} + n_{OCO} \geq 3$) account for almost 30% of the Li^+, but only account for 10% of the total displacement. We refer to these states with $n_{SO_3^-} + n_{OCO} \geq 3$ or $n_{SO_3^-} \geq 2$ as polymer-bound states.

Table S3 shows the number fraction of each state for $\lambda = 1$, 2, or 3. In all cases, a majority of Li^+ are in a polymer-bound state, however, the fraction of fully solvated and mobile, partially solvated states increases with increasing λ.

DRS provides qualitative support for these results. Figure 5(d) shows the instantaneous

concentration of the free charge carriers, which in this case are Li^+ ions. The total concentration of Li^+ in the PES12Li samples is 1.4-2 nm^{-3} (2.3-3.3 M) where the upper value corresponds to the dry polymer. DRS indicates that only a small fraction (< 0.4%) of these ions are actually acting as charge carriers at a given instant. As discussed in the SI, the physical interpretation of these quantities is difficult, so we use them to provide qualitative insights. Nevertheless, the solvent swollen samples ($\lambda > 0$) have approximately twice as many instantaneously free charge carriers as the dry material, and these charge carriers have much higher mobility than in the dry material, Figure 5(b). This is in qualitative agreement with the MD simulations, which suggest that added solvent increases the concentration of mobile Li^+.

It is evident from the analysis of coordination states from MD simulations that the two different types of polymer associations, SO_3^- and ester OCO, differ in their effects on Li^+ mobility. For example, the state with two EC coordinations and two polymer SO_3^- coordinations ($n_{EC} = 2$, $n_{SO_3^-} = 2$, $n_{OCO} = 0$) is almost ten times more common than two EC and two ester coordinations ($n_{EC} = 2$, $n_{SO_3^-} = 0$, $n_{OCO} = 2$), yet these two states contribute almost equally to the total displacement of EC. It appears that the ester associations allow Li^+ ions to be more mobile than an association to SO_3^-, presumably because SO_3^- binds to Li^+ more strongly than OCO as found in quantum chemistry calculations.[11] This presumption can be evaluated directly from the MD simulations.

In Figure 7(a) we plot the continuous association correlation function between Li^+ and EC, polymer ester, and SO_3^- groups.[41–44] This correlation function measures the fraction of Li^+ that have not broken their initial pairwise associations after some time, Δt. This correlation does not account for the full coordination environment of each Li^+, only focusing on each pairwise Li^+-oxygen association. We fit the correlation function to a stretched exponential function and extract a dissociation time, t_{dis}, for each type of association. These dissociation times are plotted as a function of λ in Figure 7(b). Notably, the dissociation time between Li^+ and SO_3^- is approximately three times longer than the dissociation time

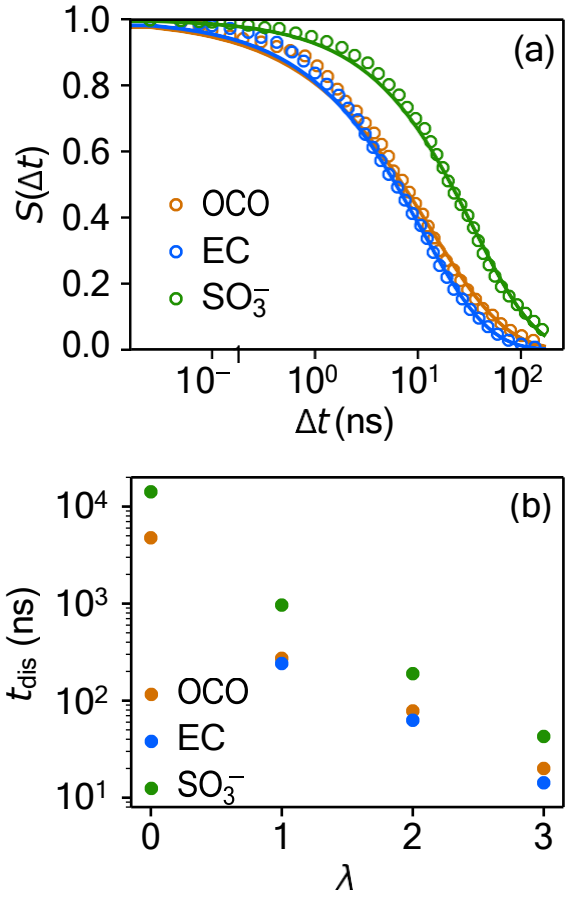

Figure 7: (a) Continuous association correlation function between Li^+ and solvent or polymer groups in amorphous layer morphology with $\lambda = 3$ at 80°C. Circles indicate data points and solid line indicates a fit to a stretched exponential. (b) Time for Li^+ to dissociate from the solvent or groups on the polymer (t_{dis}) versus amount of solvent (λ). For $1 \leq \lambda \leq 3$, t_{dis} was measured in amorphous layers. For $\lambda = 0$, t_{dis} was measured in crystalline layers.

between Li^+ and either EC or polymer ester groups. This supports the conclusion from the total displacement fraction that SO_3^- binds Li^+ more strongly than OCO.

As λ is increased from zero to three, the dissociation times t_{dis} all decrease by orders of magnitude. There are multiple contributing factors to this result. The distribution of Li^+ coordination states shifts to states that have fewer total polymer associations and are more mobile. The sulfonate groups on the polymer are also more mobile due to the enhanced polymer segmental mobility, allowing easier exchange of Li^+ with other solvating groups. Despite these multiple factors contributing to the reduced association time between SO^-_3

and Li^+, the decrease in Li^+-SO^-_3 association time with increasing solvent is consistent with the barrier reduction by partial solvation mechanism discussed in the introduction.

In addition to examining the impact on Li^+ mobility from different coordination states and types of polymer association, we can also evaluate how differences in self-assembled morphology affect Li^+ mobility. Figure 8 shows the MSD of (a) EC and (b) Li^+ in layers with $\lambda = 2$. We compare amorphous layers to crystalline layers, which are metastable. The MSD has been decomposed into parts perpendicular to the layers (red) and parallel to the layers (blue). The parallel diffusion is two dimensional, whereas the perpendicular diffusion is one dimensional. If the diffusion were isotropic then $\frac{1}{2}\langle \Delta r^2_{\parallel} \rangle = \langle \Delta r^2_{\perp} \rangle$, however we see that is not the case. The anisotropic diffusion occurs because both EC and Li^+ prefer to stay in the polar domain and thus experience confinement from the neighboring non-polar domains.

For EC, we see that this confinement effect depends on morphology. The crystalline layers (Figure 8(a), solid lines) lead to stronger anisotropy in the diffusion of EC compared to amorphous layers, (Figure 8(a) dashed lines). In the amorphous layers, the non-polar alkane groups are more mobile and allow a small amount of EC to diffuse into the non-polar domain. In contrast, the crystalline layers have non-polar alkane groups that are tightly packed such that it is hard for EC to diffuse into the non-polar block. Thus there is stronger confinement in the crystalline layers and less diffusion perpendicular to the layers compared with the amorphous layer morphology.

While EC diffusion is sensitive to morphology, the Li^+ diffusion does not seem to depend on morphology as the dashed and solid lines in Figure 8(b) nearly overlap. This indicates that the Li^+ diffusion is partially decoupled from the diffusion of EC. Because most of the Li^+ remains at the EC-polymer interface and is coordinated to both species, it is not perfectly correlated to the 'bulk' motion of the EC nor to the alkane segments.

DRS results also support the claim that Li^+ motion is not tied to the nanophase morphology. Figure 5(b) shows that for the EC-swollen sample with $\lambda = 1.8$ (dark blue circles), the slope of mobility μ versus inverse temperature $1/T$ is constant for both the disordered

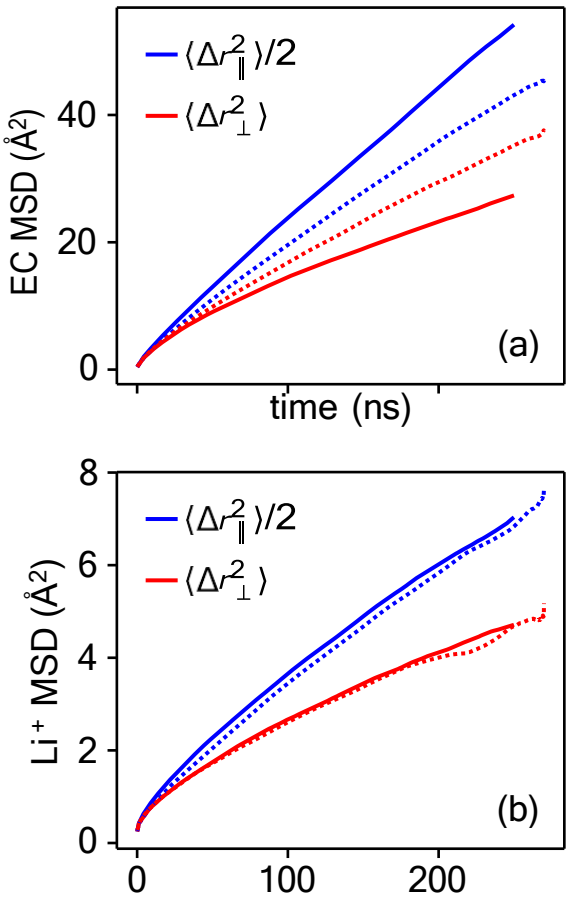

Figure 8: Mean squared displacement (MSD) of (a) EC and (b) Li^+ in layered structures with $\lambda = 2$ at 80°C from molecular dynamics. The MSD is decomposed in the directions parallel to the layers (blue) and perpendicular to the layers (red). Solid lines represent data from crystalline layers. Dotted lines represent data from amorphous layers.

morphology (open symbols) and the layered morphology (filled symbols). The constant slope across morphologies indicates that there is not a strong effect of morphology on Li^+ mobility.

Conclusions

We have demonstrated the formation of self-assembled nanoscale domains in a strictly-alternating multiblock single-ion-conducting polymer via SAXS and MD simulations. MD simulations reveal that adjacent-reentry chain packing in the layers yields domain spacings consistent with SAXS measurements. We are able to swell the material with ethylene car-

bonate and MD simulations indicate that the added ethylene carbonate partitions into the polar domain of the morphology and distorts the polar domains. The added solvent leads to orders of magnitude increased conductivity, which we attribute to the partial solvation of the Li^+ by EC that allows easier dissociation of the Li^+ from the strong binding of the sulfonate groups and therefore lowers the barrier for Li^+ diffusion. Because the Li^+ is only partially solvated by the EC at these λ values, the Li^+ diffusion primarily occurs at the solvent-polymer interface, with Li^+ typically being associated with both solvent molecules and the polymer, in contrast to the vehicular diffusion observed in organic liquid electrolytes. While experimentally we have been limited to modest solvation numbers ($\lambda \leq 1.8$), MD simulations indicate that higher solvation numbers ($\lambda \geq 2$) will lead to dramatic increases in Li^+ ion mobility due to higher EC coordination and increased number of mobile Li^+ ions. Future work will attempt to achieve higher solvation numbers λ and examine the effects of other organic solvents commonly used in battery electrolyte applications.

Acknowledgement

This work was performed at the Center for Integrated Nanotechnologies, an Office of Science User Facility operated for the U. S. Department of Energy (DOE) Office of Science. Sandia National Laboratories is a multimission laboratory managed and operated by the National Technology and Engineering Solutions of Sandia, LLC, a wholly owned subsidiary of Honeywell International, Inc., for the U.S. Department of Energy's National Nuclear Security Administration under contract DE-NA-0003525. The views expressed in the article do not necessarily represent the views of the U.S. DOE or the United States Government. BF and KIW acknowledge NSF-DMR 1904767. The authors also acknowledge use of the Dual Source and Environmental X-ray Scattering facility operated by the Laboratory for Research on the Structure of Matter at the University of Pennsylvania supported by NSF through DMR-2309043 grant. We thank Alain Plante for the use of his TGA. Funding by

the Baden-Württemberg Foundation (project “PRICON”) is gratefully acknowledged.

Supporting Information Available

Example TGA curves, temperature-dependent X-ray scattering, DRS fits, adjacent-reentry and extended chain packing examples, example radial distribution functions, coordination state distributions

References

(1) Yi, J.; Guo, S.; He, P.; Zhou, H. Status and prospects of polymer electrolytes for solid-state Li–O2 (air) batteries. *Energy Environ. Sci.* **2017**, *10*, 860–884.

(2) Chen, W.; Lei, T.; Wu, C.; Deng, M.; Gong, C.; Hu, K.; Ma, Y.; Dai, L.; Lv, W.; He, W.; Liu, X.; Xiong, J.; Yan, C. Designing Safe Electrolyte Systems for a High-Stability Lithium–Sulfur Battery. *Advanced Energy Materials* **2018**, *8*, 1702348.

(3) Lin, Y.; Huang, S.; Zhong, L.; Wang, S.; Han, D.; Ren, S.; Xiao, M.; Meng, Y. Organic liquid electrolytes in Li-S batteries: actualities and perspectives. *Energy Storage Materials* **2021**, *34*, 128–147.

(4) Timachova, K.; Watanabe, H.; Balsara, N. P. Effect of Molecular Weight and Salt Concentration on Ion Transport and the Transference Number in Polymer Electrolytes. *Macromolecules* **2015**, *48*, 7882–7888.

(5) Forsyth, M.; Porcarelli, L.; Wang, X.; Goujon, N.; Mecerreyes, D. Innovative Electrolytes Based on Ionic Liquids and Polymers for Next-Generation Solid-State Batteries. *Accounts of Chemical Research* **2019**, *52*, 686–694.

(6) Jones, S. D.; Nguyen, H.; Richardson, P. M.; Chen, Y.-Q.; Wyckoff, K. E.; Hawker, C. J.; Clément, R. J.; Fredrickson, G. H.; Segalman, R. A. Design of Poly-

meric Zwitterionic Solid Electrolytes with Superionic Lithium Transport. *ACS Central Science* **2022**, *8*, 169–175.

(7) Mecerreyes, D.; Casado, N.; Villaluenga, I.; Forsyth, M. Current Trends and Perspectives of Polymers in Batteries. *Macromolecules* **2024**, *57*, 3013–3025.

(8) Pesko, D. M.; Timachova, K.; Bhattacharya, R.; Smith, M. C.; Villaluenga, I.; Newman, J.; Balsara, N. P. Negative Transference Numbers in Poly(ethylene oxide)-Based Electrolytes. *Journal of The Electrochemical Society* **2017**, *164*, E3569.

(9) Xu, K. Navigating the minefield of battery literature. *Commun. Mater.* **2022**, *3*.

(10) Zhang, H.; Li, C.; Piszcz, M.; Coya, E.; Rojo, T.; Rodriguez-Martinez, L. M.; Armand, M.; Zhou, Z. Single lithium-ion conducting solid polymer electrolytes: advances and perspectives. *Chem. Soc. Rev.* **2017**, *46*, 797–815.

(11) Stevens, M. J.; Rempe, S. L. B. Binding of Li+ to Negatively Charged and Neutral Ligands in Polymer Electrolytes. *The Journal of Physical Chemistry Letters* **2023**, *14*, 10200–10207.

(12) Eshetu, G. G.; Mecerreyes, D.; Forsyth, M.; Zhang, H.; Armand, M. Polymeric ionic liquids for lithium-based rechargeable batteries. *Mol. Syst. Des. Eng.* **2019**, *4*, 294–309.

(13) Borodin, O.; Smith, G. D. Li^+ Transport Mechanism in Oligo(Ethylene Oxide)s Compared to Carbonates. *Journal of Solution Chemistry* **2007**, *36*, 803–813.

(14) Popovic, J.; Pfaffenhuber, C.; Melchior, J.; Maier, J. Determination of individual contributions to the ionic conduction in liquid electrolytes: Case study of LiTf/PEGDME-150. *Electrochemistry Communications* **2015**, *60*, 195–198.

(15) Liyana-Arachchi, T. P.; Haskins, J. B.; Burke, C. M.; Diederichsen, K. M.; McCloskey, B. D.; Lawson, J. W. Polarizable Molecular Dynamics and Experiments of 1,2-

Dimethoxyethane Electrolytes with Lithium and Sodium Salts: Structure and Transport Properties. *The Journal of Physical Chemistry B* **2018**, *122*, 8548–8559.

(16) Fong, K. D.; Self, J.; Diederichsen, K. M.; Wood, B. M.; McCloskey, B. D.; Persson, K. A. Ion Transport and the True Transference Number in Nonaqueous Polyelectrolyte Solutions for Lithium Ion Batteries. *ACS Central Science* **2019**, *5*, 1250–1260.

(17) Hallinan, D. T.; Balsara, N. P. Polymer Electrolytes. *Annual Review of Materials Research* **2013**, *43*, 503–525.

(18) Rank, C.; Yan, L.; Mecking, S.; Winey, K. I. Periodic Polyethylene Sulfonates from Polyesterification: Bulk and Nanoparticle Morphologies and Ionic Conductivities. *Macromolecules* **2019**, *52*, 8466–8475.

(19) Park, J.; Staiger, A.; Mecking, S.; Winey, K. I. Structure–Property Relationships in Single-Ion Conducting Multiblock Copolymers: A Phase Diagram and Ionic Conductivities. *Macromolecules* **2021**, *54*, 4269–4279.

(20) Park, J.; Staiger, A.; Mecking, S.; Winey, K. I. Sub-3-Nanometer Domain Spacings of Ultrahigh-χ Multiblock Copolymers with Pendant Ionic Groups. *ACS Nano* **2021**, *15*, 16738–16747.

(21) Park, J.; Staiger, A.; Mecking, S.; Winey, K. I. Ordered Nanostructures in Thin Films of Precise Ion-Containing Multiblock Copolymers. *ACS Central Science* **2022**, *8*, 388–393.

(22) Park, J.; Staiger, A.; Mecking, S.; Winey, K. I. Enhanced Li-Ion Transport through Selectively Solvated Ionic Layers of Single-Ion Conducting Multiblock Copolymers. *ACS Macro Letters* **2022**, *11*, 1008–1013.

(23) Yamada, Y.; Takazawa, Y.; Miyazaki, K.; Abe, T. Electrochemical Lithium Intercala-

tion into Graphite in Dimethyl Sulfoxide-Based Electrolytes: Effect of Solvation Structure of Lithium Ion. *The Journal of Physical Chemistry C* **2010**, *114*, 11680–11685.

(24) Thompson, A. P.; Aktulga, H. M.; Berger, R.; Bolintineanu, D. S.; Brown, W. M.; Crozier, P. S.; in 't Veld, P. J.; Kohlmeyer, A.; Moore, S. G.; Nguyen, T. D.; Shan, R.; G, M. J.; Tranchida, J.; Trott, C.; Plimpton, S. J. LAMMPS - a flexible simulation tool for particle-based materials modeling at the atomic, meso, and continuum scales. *Comp. Phys. Comm.* **2022**, *271*, 108171.

(25) Garcia-Melgarejo, V.; Alejandre, J.; Núñez-Rojas, E. Parametrization with explicit water of solvents used in lithium-ion batteries: cyclic carbonates and linear ethers. *J. Phys. Chem. B* **2020**, *124*, 4741–4750.

(26) Siu, S. W. I.; Pluhackova, K.; Böckmann, R. A. Optimization of the OPLS-AA Force Field for Long Hydrocarbons. *Journal of Chemical Theory and Computation* **2012**, *8*, 1459–1470.

(27) Canongia Lopes, J. N.; Pádua, A. A. H.; Shimizu, K. Molecular Force Field for Ionic Liquids IV: Trialkylimidazolium and Alkoxycarbonyl-Imidazolium Cations; Alkylsulfonate and Alkylsulfate Anions. *The Journal of Physical Chemistry B* **2008**, *112*, 5039–5046.

(28) Vigil, D. L.; Stevens, M. J.; Frischknecht, A. L. Accurate Calculation of Solvation Properties of Lithium Ions in Nonaqueous Solutions. *The Journal of Physical Chemistry B* **2023**, *127*, 8002–8008.

(29) Wu, H.; Wick, C. D. Computational investigation on the role of plasticizers on ion conductivity in poly(ethylene oxide) LiTFSI electrolytes. *Macromolecules* **2010**, *43*, 3502–3510.

(30) Leontyev, I.; Stuchebrukhov, A. Accounting for electronic polarization in non-polarizable force fields. *Phys. Chem. Chem. Phys.* **2011**, *13*, 2613–2626.

(31) Leontyev, I. V.; Stuchebrukhov, A. A. Polarizable molecular interactions in condensed phase and their equivalent nonpolarizable models. *J. Chem. Phys.* **2014**, *141*, 014103.

(32) Chaudhari, M. I.; Nair, J. R.; Pratt, L. R.; Soto, F. A.; Balbuena, P. B.; Rempe, S. B. Scaling atomic partial charges of carbonate solvents for lithium ion solvation and diffusion. *J. Chem. Theory Comput.* **2016**, *12*, 5709–5718.

(33) in 't Veld, P. J.; Rutledge, G. C. Temperature-dependent elasticity of a semicrystalline interphase composed of freely rotating chains. *Macromolecules* **2003**, *36*, 7358–7365.

(34) in 't Veld, P. J. EMC: Enhanced Monte Carlo. https://montecarlo.sourceforge.net/emc/, Accessed: 2022-10-01.

(35) Stukowski, A. Visualization and analysis of atomistic simulation data with OVITO–the Open Visualization Tool. *Modelling and Simulation in Materials Science and Engineering* **2009**, *18*, 015012.

(36) Buitrago, C. F.; Bolintineanu, D. S.; Seitz, M. E.; Opper, K. L.; Wagener, K. B.; Stevens, M. J.; Frischknecht, A. L.; Winey, K. I. Direct Comparisons of X-ray Scattering and Atomistic Molecular Dynamics Simulations for Precise Acid Copolymers and Ionomers. *Macromolecules* **2015**, *48*, 1210–1220.

(37) Tsubakihara, S.; Nakamura, A.; Yasuniwa, M. Hexagonal Phase of Polyethylene Fibers under High Pressure. *Polymer Journal* **1991**, *23*, 1317–1324.

(38) Trigg, E. B.; Stevens, M. J.; Winey, K. I. Chain Folding Produces a Multilayered Morphology in a Precise Polymer: Simulations and Experiments. *Journal of the American Chemical Society* **2017**, *139*, 3747–3755.

(39) Fragiadakis, D.; Dou, S.; Colby, R. H.; Runt, J. Molecular mobility and Li+ conduction in polyester copolymer ionomers based on poly(ethylene oxide). *The Journal of Chemical Physics* **2009**, *130*, 064907.

(40) Chen, Q.; Tudryn, G. J.; Colby, R. H. Ionomer dynamics and the sticky Rouse modela). *Journal of Rheology* **2013**, *57*, 1441–1462.

(41) Luzar, A.; Chandler, D. Effect of environment on hydrogen bond dynamics in liquid water. *Phys. Rev. Lett.* **1996**, *76*, 928–931.

(42) Müller-Plathe, F. Microscopic dynamics in water-swollen poly(vinyl alcohol). *J. Chem. Phys.* **1998**, *108*, 8252–8263.

(43) Chandra, A. Effects of ion atmosphere on hydrogen-bond dynamics in aqueous electrolyte solutions. *Phys. Rev. Lett.* **2000**, *85*, 768–771.

(44) Zhao, W.; Leroy, F.; Heggen, B.; Zahn, S.; Kirchner, B.; Balasubramanian, S.; Müller-Plathe, F. Are there stable ion-pairs in room-temperature ionic liquids? Molecular dynamics simulations of 1-n-butyl-3-methylimidazolium jexafluorophosphate. *J. Am. Chem. Soc.* **2009**, *131*, 15825–15833.

TOC Graphic

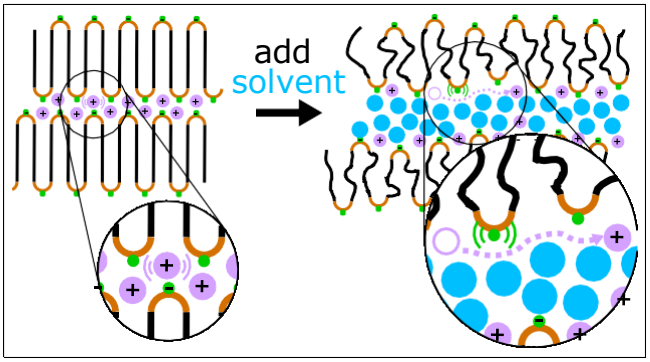

Supporting Information:

Partial solvation of lithium ions enhances conductivity in a nanophase-separated polymer electrolyte

Daniel L. Vigil,[†] Benjamin T. Ferko,[‡] Anne Saumer,[¶] Stefan Mecking,[¶] Mark J. Stevens,[*,†] Karen I. Winey,[*,‡,§] and Amalie L. Frischknecht[*,†]

†*Center for Integrated Nanotechnologies, Sandia National Laboratories, Albuquerque, NM, 87185*

‡*Department of Materials Science, University of Pennsylvania*

¶*Department of Chemistry, University of Konstanz, 78457 Konstanz, Germany*

§*Department of Chemical and Biomolecular Engineering, University of Pennsylvania*

E-mail: msteve@sandia.gov; winey@seas.upenn.edu; alfrisc@sandia.gov

Thermogravimetric Analysis (TGA) Data for Dry and EC-Swollen PES12Li Membranes

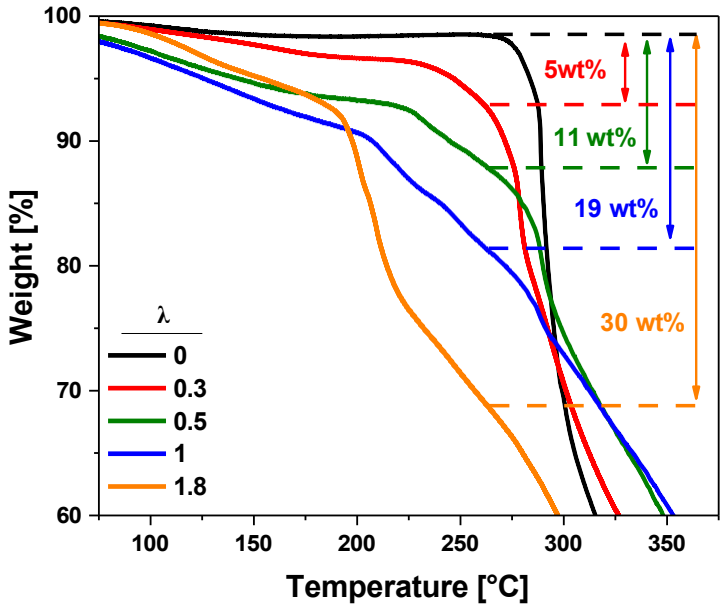

Figure S1: Thermogravimetric analysis (TGA) data for the samples in this investigation. The high boiling point of EC (T_b = 248) prevents the formation of a well-defined plateau upon solvent evaporation. The solvent weight fraction for each sample is taken near 260°C before the onset of degradation in the dry polymer, and λ values are reported with reduced precision.

Table S1: Membrane preparation conditions and resulting amount of solvent uptake as measured by TGA. The first column indicates whether the dry membrane was annealed before being swollen in solvent.

Post-press annealed?	swelling time (min)	λ
Y	0	0
Y	2	0.25
N	20	0.5
N	360	1
Y	360	1.8

Dipolar Relaxation Fitting

Ionic conduction adds a frequency independent contribution to the measured dielectric loss spectra that can obscure dipolar relaxations. The derivative formalism can be applied to remove the effects of conduction from the imaginary permittivity spectra:[S1–S4]

$$\epsilon''_{\text{der}} = -\frac{\pi}{2}\frac{\delta\epsilon'(\omega)}{\delta \ln \omega} \tag{S1}$$

Here, the permittivity spectra of both swollen and dry systems were satisfactorily fit by a single Havriliak-Negami (HN) function and a power law for electrode polarization over the temperature range of interest. The fitting function is given as:

$$\epsilon''_{\text{der}} = -\frac{\pi}{2}\frac{\delta\epsilon'_{\text{HN}}(\omega)}{\delta \ln \omega} + A\omega^{-s} \tag{S2}$$

with

$$\epsilon'_{\text{HN}} = \text{Re}\left[\frac{\Delta\epsilon}{(1 + (i\omega\tau_0)^a)^b}\right] \tag{S3}$$

$$\frac{\delta\epsilon'_{\text{HN}}(\omega)}{\delta \ln \omega} = -\frac{ab\Delta\epsilon(\omega\tau)^a \cos\left(\frac{a\pi}{2} - (1+b)\theta_{\text{HN}}\right)}{\left(1 + 2(\omega\tau_0)^a \cos\left(\frac{\pi a}{2}\right) + (\omega\tau_0)^{2a}\right)^{\frac{1+b}{2}}} \tag{S4}$$

$$\theta_{\text{HN}} = \tan^{-1}\left[\frac{\sin\left(\frac{\pi a}{2}\right)}{(\omega\tau_0)^a + \cos\left(\frac{\pi a}{2}\right)}\right] \tag{S5}$$

where A and s are constants related to electrode polarization, $\Delta\epsilon$ is the dielectric strength, τ_0 is the HN relaxation time, and a and b are shape parameters.[S2,S4,S5] The characteristic timescale (τ_{max}) or frequency (ω_{max}) associated with the measured dipolar relaxation is then determined by:[S2,S5]

$$\tau_{\text{max}} = \frac{1}{\omega_{\text{max}}} = \tau_0 \left[\frac{\sin\left(\frac{\pi ab}{2(1+b)}\right)}{\sin\left(\frac{\pi a}{2(1+b)}\right)}\right]^{\frac{1}{a}} \tag{S6}$$

Figure S2 shows representative fits for all three measured samples.

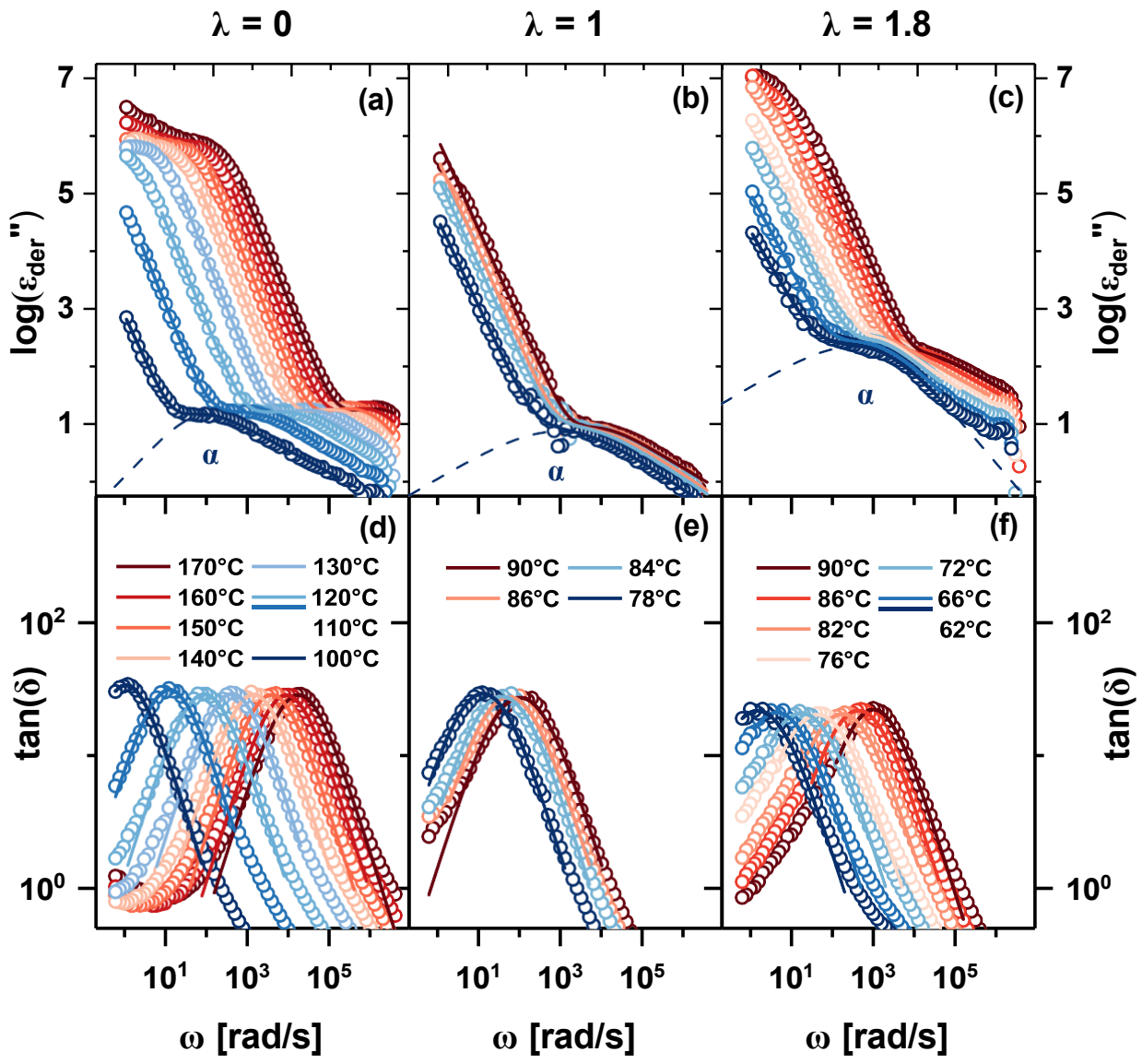

Figure S2: Representative data (open circles) and fits (solid lines) to the conductivity-free permittivity and loss tangent spectra for PES12Li swollen with EC at (a,d) λ = 0 (b,e) λ = 1 and (c,f) λ = 1.8. Dashed curves display the α relaxation term of the HN function for the lowest temperature fit.

Electrode Polarization Analysis

The Macdonald-Coelho model for electrode polarization (EP) has been previously used in the literature to quantify the simultaneously conducting free ion concentration and mobility in single-ion containing polymers.[S2,S3,S6,S7] This model calculates the simultaneously conducting free ion concentration p as:

$$p = \frac{1}{\pi l_b L^2} \left(\frac{\tau_{EP}}{\tau_\sigma} \right)^2 \tag{S7}$$

where τ_{EP} and τ_σ are the timescales associated with electrode polarization and conductivity respectively, l_B is the Bjerrum length, and L is the spacing between electrodes.[S1,S6] The EP model solves the Poisson-Boltzmann equation which requires the result to be instantaneous.[S3] Additionally, the simultaneously conducting free ion concentration has been suggested to represent the concentration of ions that are separated by at least the Bjerrum length from their respective counterions.[S3,S8] For these reasons, the reported values of the simultaneously conducting free ion concentration are vanishingly small when compared to the total ion concentration or measurements made by other techniques.[S8] By assuming only one charged species participates in conduction, the EP model permits the calculation of the free ion mobility μ as:

$$\mu = \frac{eL^2\tau_\sigma}{4\tau_{EP}^2 k_B T} \tag{S8}$$

where e is the elementary charge, k_B is the Boltzmann constant, and T is temperature.[S1,S6] Therefore, calculation of both p and μ are determined from τ_{EP} and τ_σ. These timescales are most easily determined by fitting the loss tangent spectra.[S6] Although the Macdonald-Coelho method models EP as a simple Debye relaxation, many polymeric systems observe broadened relaxations.[S9] This broadening was observed in the loss tangent spectra for the dry material and became increasingly broad upon swelling. To account for this, the loss tangent spectra was instead fit to a Cole-Cole relaxation function which accounts for broadening with an

additional parameter α:[S9]

$$\tan(\delta) = \left[\frac{1}{(\omega\tau_0)^{1-\alpha}\cos\left(\frac{\alpha\pi}{2}\right)} + \tan\left(\frac{\alpha\pi}{2}\right) + \frac{\tau_\sigma}{\tau_{EP}} \frac{(\omega\tau_0)^{1-\alpha}}{\cos\left(\frac{\alpha\pi}{2}\right)} \right]^{-1} \tag{S9}$$

$$\tau_0 = \tau_\sigma^{\frac{\alpha}{2(\alpha-1)}} \tau_{EP}^{\frac{(\alpha-2)}{2(\alpha-1)}} \tag{S10}$$

Once τ_σ has been determined, the static dielectric constant ϵ_S is obtained by the definition of τ_σ:

$$\tau_\sigma \triangleq \frac{\epsilon_S \epsilon_0}{\sigma_{DC}} \tag{S11}$$

where ϵ_0 is the permittivity of free space and σ_{DC} is the DC conductivity of the sample.[S1] Representative fits for each sample are shown in Figure S2.

The EP model was not developed for microphase separated materials but has been successfully applied to such systems in the past.[S3,S10] The polar domains are expected to preferentially wet the electrodes and the length scale probed during the measurement is on the order of 1 nm.[S10,S11] At this length scale, the probed material is effectively homogeneous. Additionally, the EP model assumes noninteracting charges. Although the morphology of PES12Li is comprised of intentionally concentrated ionic channels, few ions are instantaneously participating in EP (< 0.1%) such that they are not expected to be interacting. Interactions between charges manifests as nonlinear electrode polarization. Colby and coworkers have suggested a dimensionless number for validating electrode polarization linearity that has been experimentally validated.[S3,S12] The condition for linearity is given as:

$$\frac{\tau_{EP} V \sigma_{DC} l_B^2}{Le} < 1 \tag{S12}$$

where V is the applied AC amplitude.[S3] Table S2 gives the value of this quantity for both the dry and swollen samples investigated in this work. All samples satisfy the linearity criteria over the temperature range studied, suggesting this assumption holds.

Finally, a major criticism of the EP model is that the results are dependent on both the

Table S2: Dimensionless parameter at the indicated temperature as a function of solvation number in EC swollen PES12Li. Similar values were calculated over the entire investigated temperature range.

λ	$\frac{t_{EP} V \sigma_{DC} l^2}{Le \quad B}$	T (°C)
0	0.118	100
1	0.096	80
1.8	0.013	80

chemistry and roughness of the electrodes. [S3,S13,S14] This dependence has been considered by preparing the polished stainless steel electrodes in the same way for all samples. It should be noted that Colby and coworkers have reported that stainless steel electrodes consistently yield smaller values of p compared with polished brass electrodes.[S3] Because of this material dependence and the many assumptions of the model, it is emphasized that the calculations should be interpreted qualitatively.

Conductivity Measurement for Several Temperature Cycles

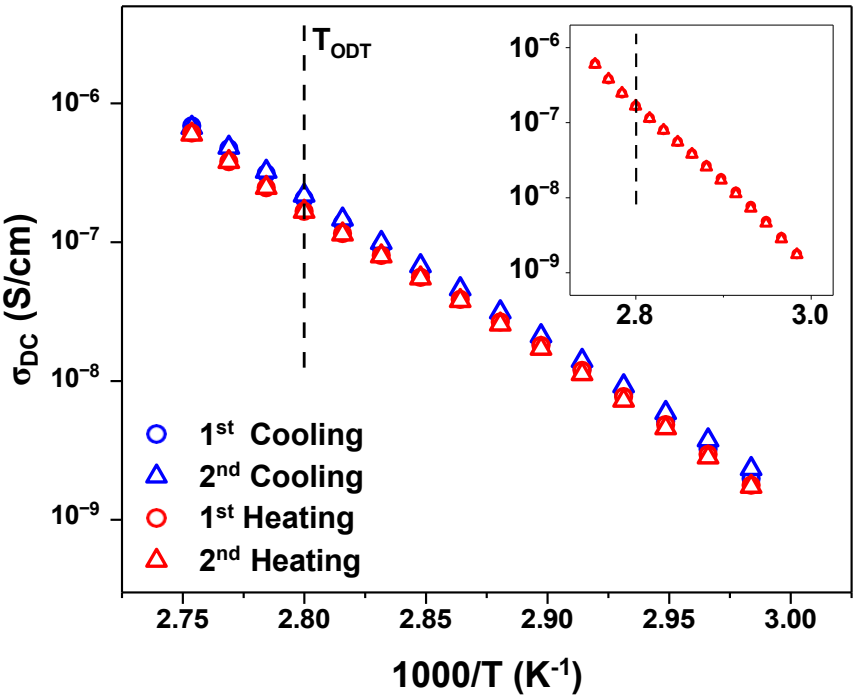

Figure S3: Measured conductivity of EC swollen PES12Li at λ = 1.8 with data taken on heating or cooling. Data is shown for two complete heating and cooling cycles. The slight hysteresis is attributed to the order-disorder transition observed in this material. Inset: Data for the heating cycles only. The data is overlapping.

Temperature-Dependent X-ray Scattering Data

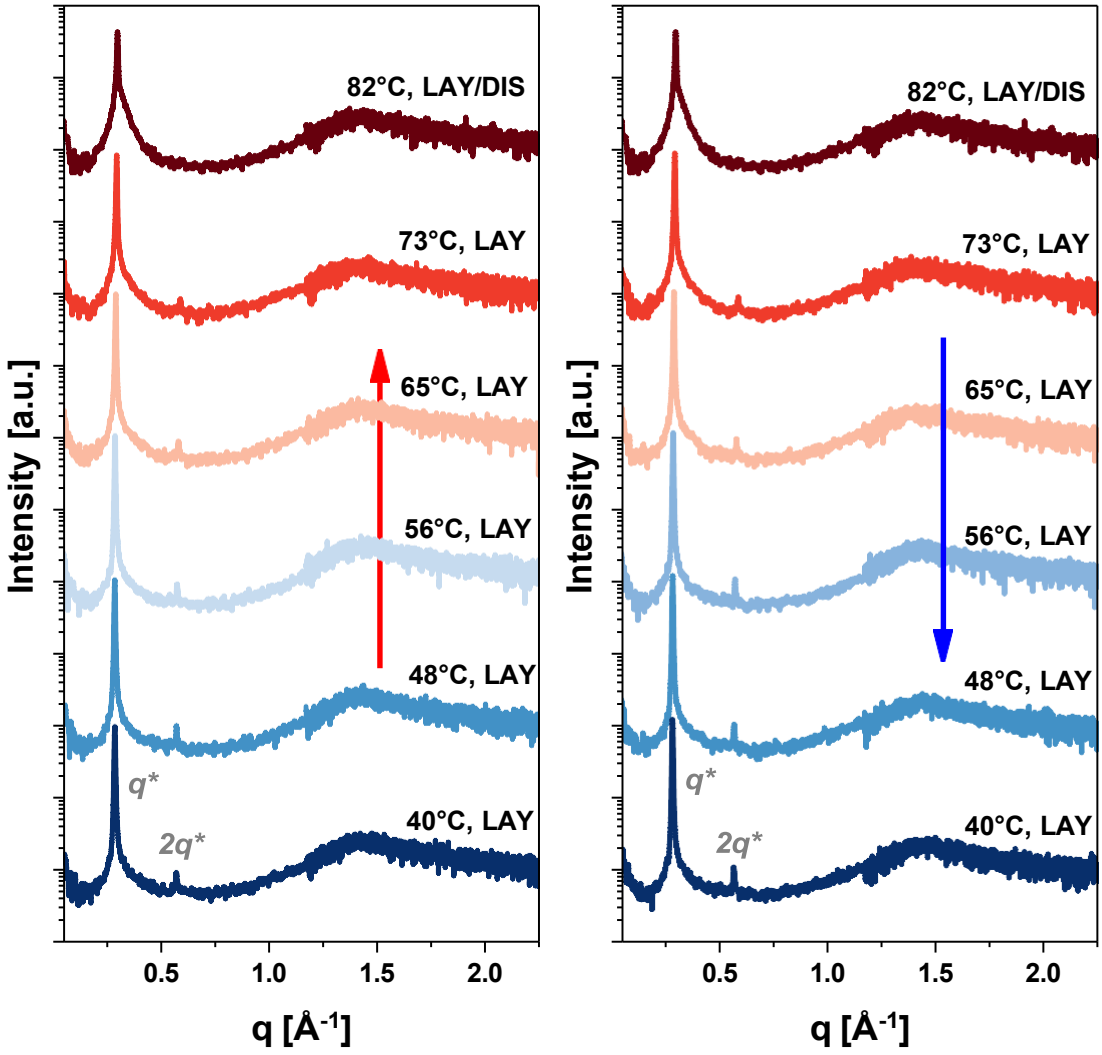

Figure S4: X-ray scattering data for EC swollen PES12Li at λ = 1.8 with collections taken on heating (left) and cooling (right). Both layered (LAY) and disordered layered (LAY/DIS) morphologies were observed. Morphological assignments are indicated with each temperature.

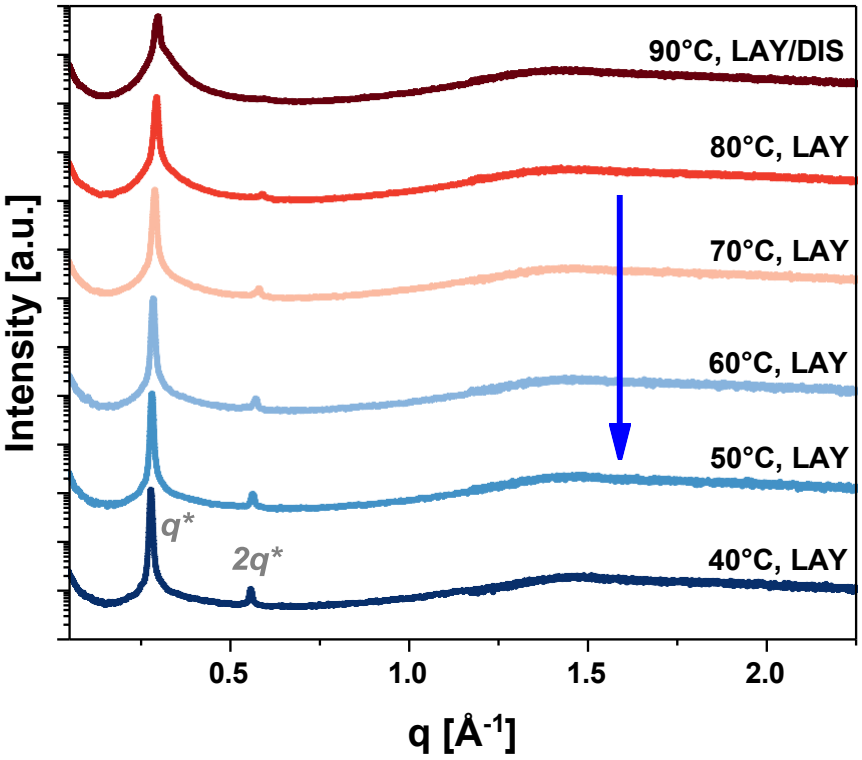

Figure S5: Temperature dependent X-ray scattering data for EC swollen PES12Li at $\lambda = 1$ taken on cooling. Layered (LAY) and disordered layered (LAY/DIS) morphology assignments are listed with each temperature.

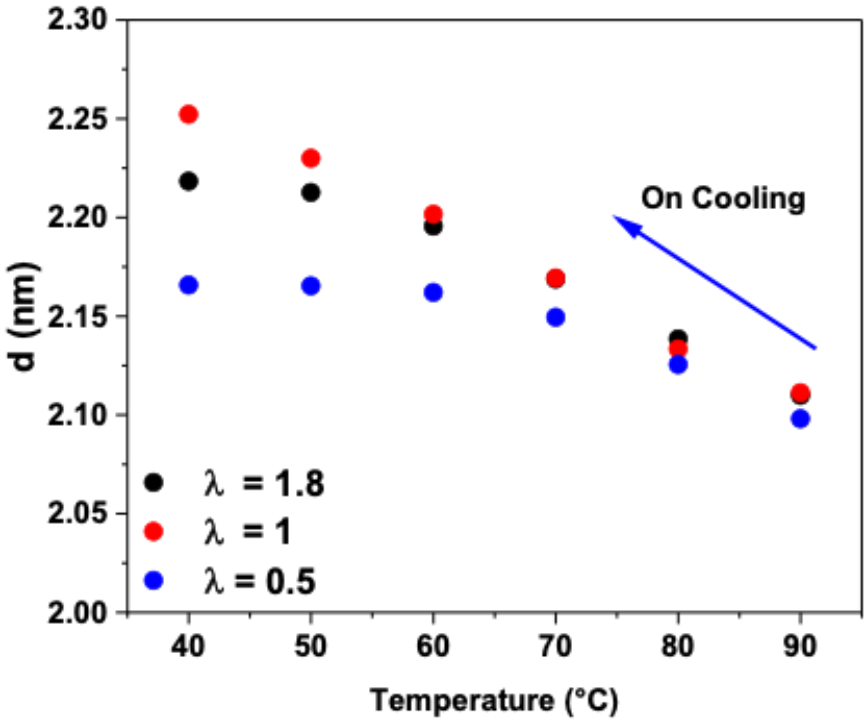

Figure S6: Domain spacing as determined by X-ray scattering versus temperature for EC swollen PES12Li with three different levels of added solvent λ.

Distribution of sulfonate groups in a polymer layer

Figure S7 shows the probability density of finding the *n*th nearest sulfur from another sulfur at a given distance *r*, analogous to a nearest-neighbor distribution between sulfurs. This provides insight into the spatial distance between sulfur groups. For the dry material with $\lambda = 0$, the distribution for the five nearest sulfurs are peaked near each other in the range $4\ \text{Å} < r < 6\ \text{Å}$. As λ is increased, the distributions for the fourth and fifth nearest sulfurs, $P_4(r)$ and $P_5(r)$, have a peak that shifts to much larger values $r > 8\ \text{Å}$ and the distributions become very broad. The first and second nearest sulfurs have distributions that are peaked near the same position in the solvent-swollen samples as in the dry material. This indicates that each SO_3^- group has a few neighboring SO_3^- groups that remain nearby as λ increases, while other SO_3^- groups that were nearby in the dry state are further away in the solvent swollen state due to lateral swelling. This can be seen visually in the snapshots from MD simulations also shown in Figure S7. At $\lambda = 0$ the SO_3^- groups (green) are densely packed on the polymer layer. As λ increases, the areal density of SO_3^- groups decreases due to lateral swelling. Some holes in the alkyl layer also form for $\lambda \geq 2$ as the solvent begins to penetrate the non-polar domain. Despite the lower areal density of SO_3^- groups, the SO_3^- groups remain somewhat clustered so that there are still a few other SO_3^- groups nearby each SO_3^-. This is consistent with the nearest sulfur distributions discussed previously. The SO_3^- groups are not uniformly distributed in the plane of the layer for $\lambda \geq 2$ to accommodate the swollen layer size and tendency for SO_3^- groups to cluster.

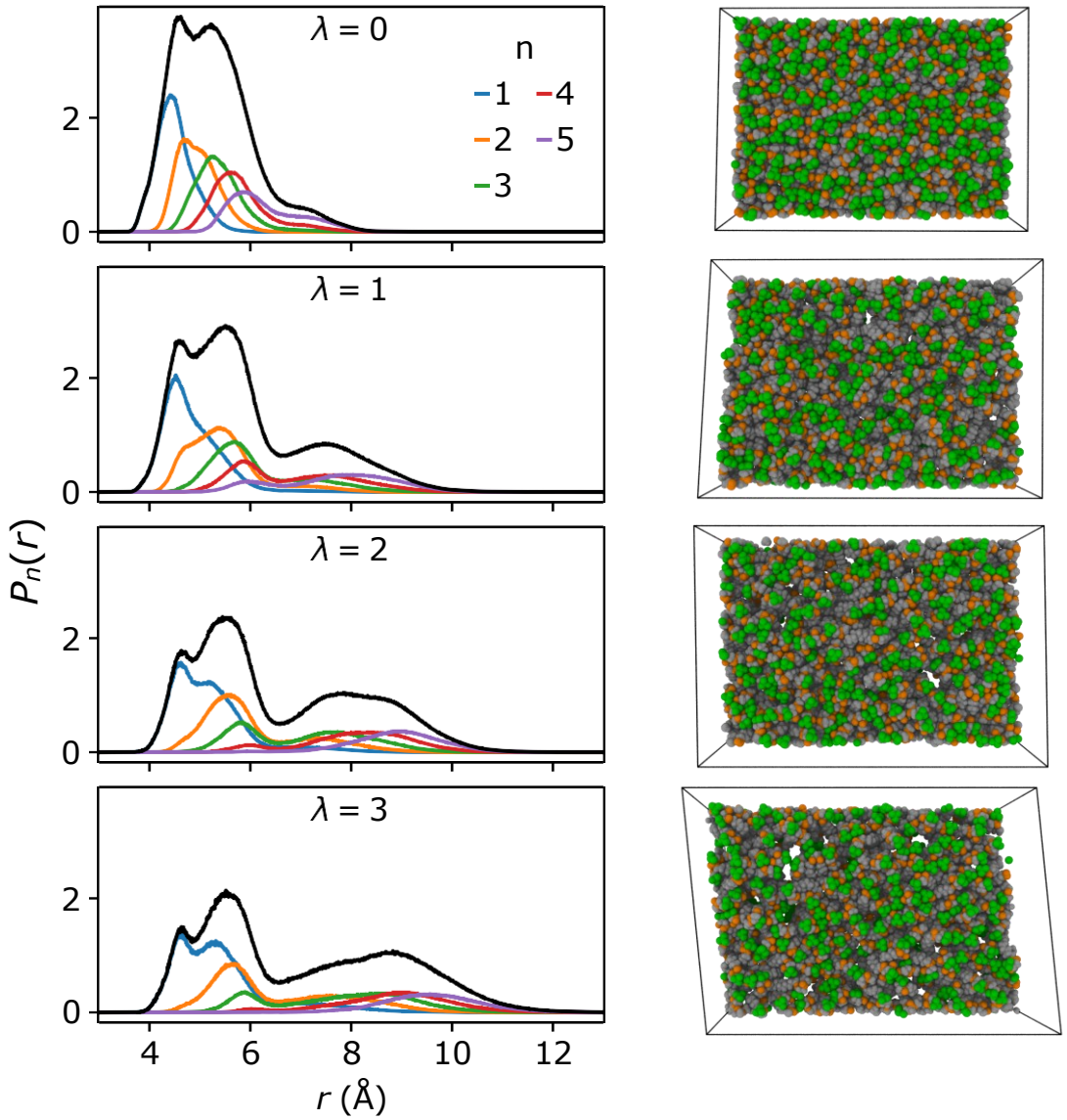

Figure S7: Probability density $P_n(r)$ of finding the nth nearest sulfur from another sulfur at a given distance r in layers at 80 °C. The probability density for the first through fifth nearest neighbors are shown with colored curves while the black curve indicates the sum of the five colored curves. For λ = 0 the layers are crystalline, but all other layers are amorphous. Snapshots from MD simulations show a single polymer layer with all solvent and Li^+ removed. Alkane segments are shown in gray, sulfonate groups are shown in green, and ester groups are shown in orange.

Extended versus adjacent reentry chain packing

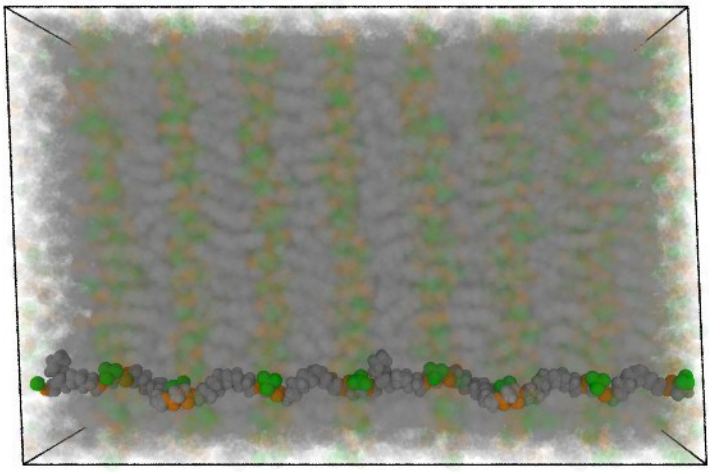

Figure S8: A single chain (dark colors) in the extended chain conformation in a crystalline layered morphology, with the rest of the system shown as semi-transparent.

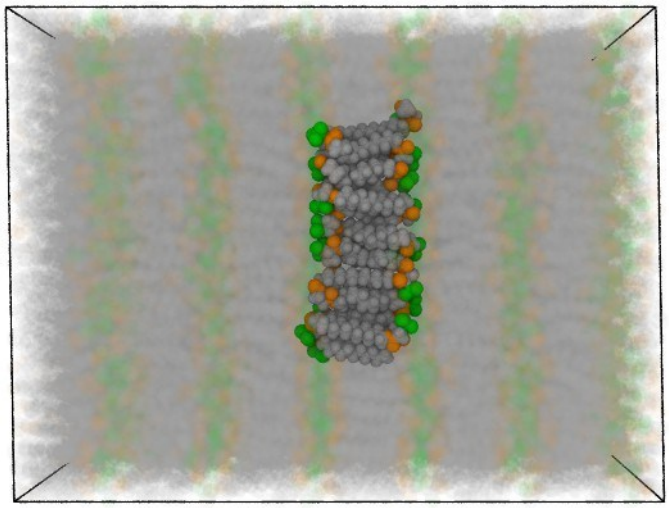

Figure S9: A single chain (dark colors) in the adjacent reentry conformation in a crystalline layered morphology, with the rest of the system shown as semi-transparent.

Radial distribution functions

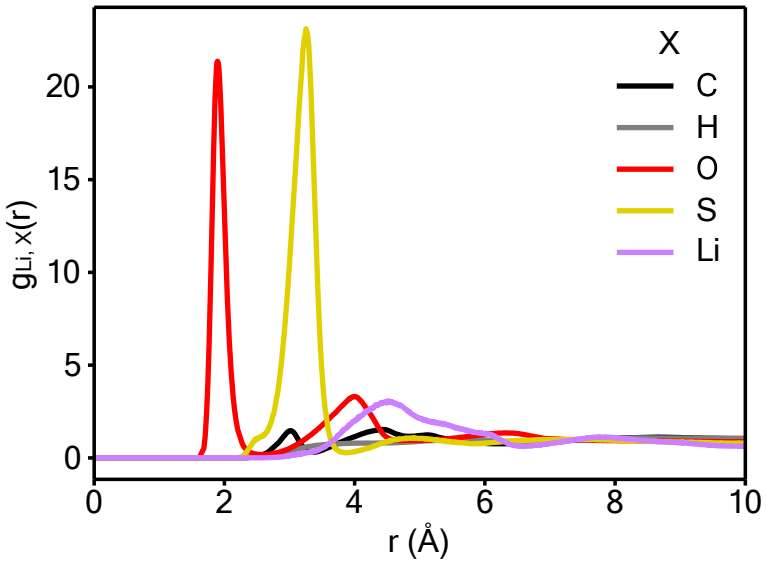

Figure S10: Radial distribution function between Li^+ and all other elements in a sample with λ = 1 and disordered aggregate morphology at 80° C.

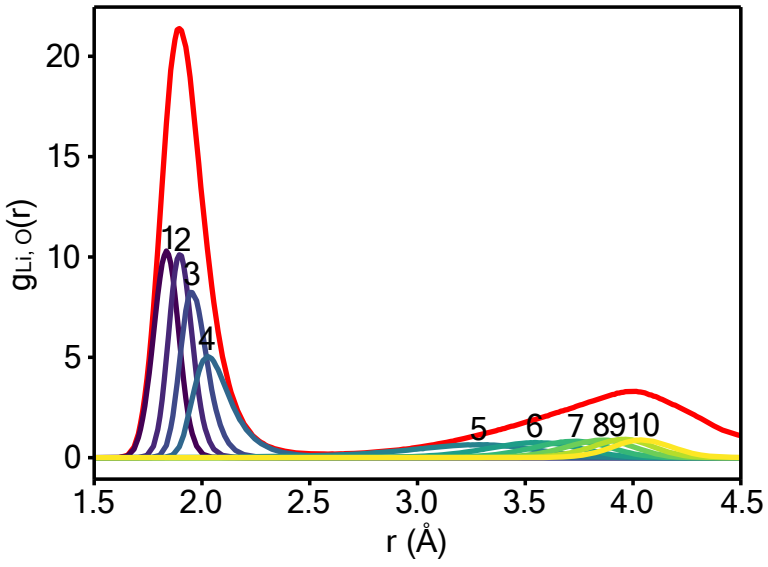

Figure S11: Neighborship-ordered radial distribution functions (numbered curves) between Li^+ and all oxygen atoms in the systems for a sample with disordered morphology and λ = 1 at 80° C (same as Figure S10). Red line is the total radial distribution function between Li^+ and oxygen.

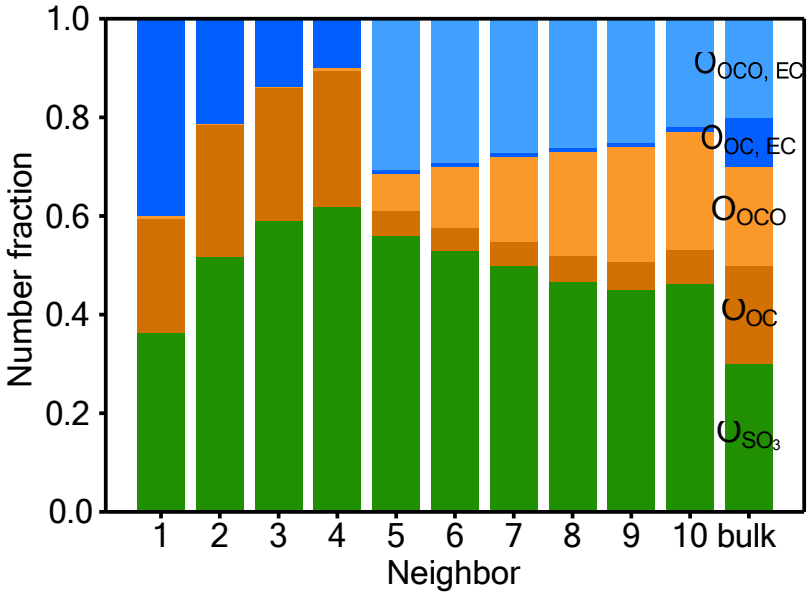

Figure S12: Composition of each neighborship ordered radial distribution function from Figure S11. The primary solvation shell of (first four neighbors) is composed almost exclusively of carbonyl oxygens from the polymer and solvent EC, as well as polymer sulfonate oxygens. The secondary solvation shell (neighbors > 5) are dominated by sulfonate oxygens and etherial carbonate/ester oxygens from EC and the polymer. Bulk indicates the number fraction of each oxygen type averaged across the entire simulation box.

Table S3: Number fraction of Li^+ with a given number of EC, SO_3^-, and ester (OCO) coordinations in amorphous layers for various swelling ratios λ at 80 °C.

n_{EC}	$n_{SO_3^-}$	n_{OCO}	Number fraction		
			$\lambda = 1$	$\lambda = 2$	$\lambda = 3$
0	4	0	0.043	0.003	0.001
0	3	1	0.112	0.039	0.019
0	2	2	0.110	0.027	0.015
0	1	3	0.013	0.004	0.002
1	3	0	0.148	0.113	0.094
1	2	1	0.241	0.209	0.117
1	1	2	0.090	0.067	0.042
2	2	0	0.078	0.191	0.214
2	1	1	0.079	0.152	0.137
2	0	2	0.013	0.022	0.023
3	1	0	0.012	0.099	0.200
3	0	1	0.004	0.025	0.051
4	0	0	0.001	0.013	0.054

References

(S1) Choi, U. H.; Ye, Y.; Salas de la Cruz, D.; Liu, W.; Winey, K. I.; Elabd, Y. A.; Runt, J.; Colby, R. H. Dielectric and Viscoelastic Responses of Imidazolium-Based Ionomers with Different Counterions and Side Chain Lengths. Macromolecules **2014**, 47, 777–790.

(S2) Choi, U. H.; Lee, M.; Wang, S.; Liu, W.; Winey, K. I.; Gibson, H. W.; Colby, R. H. Ionic Conduction and Dielectric Response of Poly(imidazolium acrylate) Ionomers. Macromolecules **2012**, 45, 3974–3985.

(S3) Tudryn, G. J.; Liu, W.; Wang, S.-W.; Colby, R. H. Counterion Dynamics in Polyester-Sulfoante Ionomers with Ionic Liquid Counterions. Macromolecules **2011**, 44, 3572–3582.

(S4) Wübbenhorst, M.; van Turnhout, J. Analysis of complex dielectric spectra. I. One-dimensional derivative techniques and three-dimensional modelling. Journal of Non-Crystalline Solids **2002**, 305, 40–49.

(S5) Park, J.; Staiger, A.; Mecking, S.; Winey, K. I. Enhanced Li-Ion Transport through Selectively Solvated Ionic Layers of Single-Ion Conducting Multiblock Copolymers. ACS Macro Letters **2022**, 11, 1008–1013.

(S6) Klein, R. J.; Zhang, S.; Dou, S.; Jones, B. H.; Colby, R. H.; Runt, J. Modeling electrode polarization in dielectric spectroscopy: Ion mobility and mobile ion concentration of single-ion polymer electrolytes. The Journal of Chemical Physics **2006**, 124, 144903.

(S7) Kuray, P.; Mei, W.; Sheffield, S. E.; Sengeh, J.; Pulido, C. R. F.; Capparelli, C.; Hickey, R. J.; Hickner, M. A. Ion Transport in Solvated Sodium-Ion Conducting Gel Polymer Electrolytes. Frontiers in Energy Research **2020**, 8.

(S8) Fragiadakis, D.; Dou, S.; Colby, R. H.; Runt, J. Molecular Mobility, Ion Mobility, and Mobile Ion Concentration in Poly(ethylene oxide)-Based Polyurethane Ionomers. Macromolecules **2008**, 41, 5723–5728.

(S9) Wang, S.-W.; Liu, W.; Colby, R. H. Counterion Dynamics in Polyurethane-Carboxylate Ionomers with Ionic Liquid Counterions. Chemistry of Materials **2011**, 23, 1862–1873.

(S10) Tudryn, G. J.; O'Reilly, M. V.; Dou, S.; King, D. R.; Winey, K. I.; Runt, J.; Colby, R. H. Molecular Mobility and Cation Conduction in Polyether–Ester–Sulfonate Copolymer Ionomers. Macromolecules **2012**, 45, 3962–3973.

(S11) Park, J.; Staiger, A.; Mecking, S.; Winey, K. I. Ordered Nanostructures in Thin Films of Precise Ion-Containing Multiblock Copolymers. ACS Central Science **2022**, 8, 388–393.

(S12) Wang, Y.; Sun, C.-N.; Fan, F.; Sangoro, J. R.; Berman, M. B.; Greenbaum, S. G.; Zawodzinski, T. A.; Sokolov, A. P. Examination of methods to determine free-ion diffusivity and number density from analysis of electrode polarization. Phys. Rev. E **2013**, 87, 042308.

(S13) Sangoro, J. R.; Serghei, A.; Naumov, S.; Galvosas, P.; Kärger, J.; Wespe, C.; Bordusa, F.; Kremer, F. Charge transport and mass transport in imidazolium-based ionic liquids. Phys. Rev. E **2008**, 77, 051202.

(S14) Pajkossy, T. Impedance spectroscopy at interfaces of metals and aqueous solutions — Surface roughness, CPE and related issues. Solid State Ionics **2005**, 176, 1997–2003, International Workshop on Impedance Spectroscopy for Characterisation of Materials and Structures.